Thin-film solar cells exceeding 22% solar cell efficiency: An overview on CdTe-, Cu(In,Ga)Se$_2$-, and perovskite-based materials

Michael Powalla, Stefan Paetel, Erik Ahlswede, Roland Wuerz, Cordula D. Wessendorf, and Theresa Magorian Friedlmeier

Zentrum für Sonnenenergie-und Wasserstoff-Forschung Baden-Württemberg (ZSW), 70563 Stuttgart, Germany

Already, several technologies of polycrystalline thin-film photovoltaic materials have achieved certified record small-cell power conversion efficiencies exceeding 22%. They are CdTe, Cu(In,Ga)(S,Se)$_2$ (CIGS), and metal halide perovskite (PSC), each named after the light-absorbing semiconductor material. Thin-film solar cells and modules require very little active material due to their very high absorption coefficient. Efficient production methods with low materials waste, moderate temperatures, attractive cost structures, and favorable energy pay-back times will play a strong role in market development as thin-film technologies reach full maturity, including mass production and the standardization of production machineries. In fact, the first two technologies have already been developed up to the industrial scale with a market share of several GW. In this review article, we outline similarities and differences between these high-efficiency thin-film technologies from both the materials and the industrial point of view. We address the materials characteristics and device concepts for each technology, including a description of recent developments that have led to very high efficiency achievements. We provide an overview of the CIGS industry players and their current status. The newcomer PSC has demonstrated its potential in the laboratory, and initial efforts in industrial production are underway. A large number of laboratories are experimenting through a wide range of options in order to optimize not only the efficiency but also stability, environmental aspects, and manufacturability of PSC. Its high efficiency and its high bandgap make PSC particularly attractive for tandem applications. An overview of all these topics is included here along with a list of materials configurations. *Published by AIP Publishing.*
https://doi.org/10.1063/1.5061809

TABLE OF CONTENTS

I. INTRODUCTION

This review article will cover the exciting last decade during which the quality of polycrystalline thin-film solar cells has made outstanding progress, leading to record small-cell power conversion efficiencies (PCEs) exceeding 22%. We will outline similarities and differences between the high-efficiency thin-film technologies CdTe, $Cu(In,Ga)(S,Se)_2$ (CIGS), and metal halide perovskite (PSC), each named after the light-absorbing semiconductor material. The first two technologies have already been developed up to the industrial scale, while initial efforts in industrial production are underway for the newcomer PSC.

Even though the photovoltaic (PV) module market is dominated by the silicon wafer-based technology, the market volume is growing rapidly and the contribution of thin-film manufacturers in the CdTe and CIGS technologies is also expanding significantly if not quite proportionally. In contrast to wafer-based modules where single cells are mechanically assembled to form a module, thin-film modules are generally processed directly on the large area. Efficiencies of small laboratory-based cells exceed 22% and are at a similarly high level as their multicrystalline silicon counterparts. However, there are some losses in efficiency when comparing full-sized modules with small cells. One reason is that most of the very new findings which lead to record efficiencies in the laboratory are not yet fully implemented in production technology at the large-area scale. It is expected that over time, the technical challenges of translating the high laboratory cell efficiencies to the module production level can be solved. However, even with the production technologies available from equipment suppliers today, thin-film technologies are a worthwhile alternative to wafer-based technologies because they combine low-cost production techniques with high efficiency and energy yield for photovoltaic power generation.

Thin-film solar cells and modules differ significantly from the silicon wafer-based technology because the sunlight-absorbing compounds (so-called "absorbers") are direct semiconductors with high optical absorption coefficients, enabling complete absorption of the incoming sunlight within a thickness of less than 3 μm. The materials are typically p-type and are combined with suitable n-type materials (so-called "windows," since they have a larger bandgap which transmits photons to the absorber) to form a p-n-heterojunction structure to generate an intrinsic electric field. The very thin structures require a mechanical support (substrate) which is typically a pane of glass but could also be something else like, e.g., a flexible metal or polymer foil. Different layer stacks are coated on the substrate by various thin-film coating methods by vacuum-based processes like sputtering or thermal evaporation or by liquid-based processes like in a chemical bath or an ink-like coating procedure. The stack sequence depends largely on the compatibility of processing conditions with the underlying layers and substrate.

Figures 1(a)–1(c) show the generic presentation of thin-film solar cells in typical substrate and superstrate configurations. The highest-efficiency process sequence generally determines which configuration is chosen although other design factors may indicate an alternative. CdTe-based modules are fabricated in the superstrate structure, with the layers being deposited onto the front glass, starting with the transparent conductive oxide (TCO) front contact. The back contact has very specific materials requirements which are difficult to meet in a substrate configuration. For CIGS, the reactivity of the absorber layer deposition process leads to best results in the substrate configuration in combination with molybdenum as a back contact. The PSC technology employs only low-temperature processes and hence allows both substrate and superstrate configurations; the superstrate setup is most common. The finished modules can be encapsulated with another glass pane or a protective foil to protect them from the elements. Completely flexible modules are possible with a flexible substrate and a flexible protective front coating or foil.

The thin-film PV technologies offer a wide scope of design opportunities. They have a homogeneous appearance which makes them particularly attractive for building integration, also in combination with specific façade design elements. As a result of the monolithic integration technique, module dimensions are not confined to any integers of a cell size and can be adjusted to any shape. The electrical output parameters can be customized within a large range of values by modifying the number of cells and their width. Regarding efficiency, the chalcogenide-compound-based modules (CdTe and CIGS) are approaching those of multicrystalline silicon modules. Perovskite-based solar cells demonstrate similarly high small-area cell efficiencies in the lab. Due to their wide bandgap, they represent an ideal option as top cells in a thin-film tandem device. For this purpose, both front and back contacts have transparency requirements. This semitransparent configuration has a high transmittance for photons with an energy below the energy bandgap, which can then be used by the bottom cell in a tandem device.

The important feature of the compound semiconductor systems, which facilitates the highest potentially achievable conversion efficiencies, is the possibility to design and modify the absorber layer properties by adjusting their composition. These solid solutions enable bandgap gradients within the absorber, as well as the possibility to adjust the band alignment in a heterojunction. The specific variations also affect material properties such as charge carrier concentration and phase stability. The chalcogenide alloy systems presently used in the II-VI compounds include combinations of Zn and Cd with S, Se, and/or Te (e.g., CdTe). In the chalcopyrite I-III-VI_2 system, Cu and Ag are typically paired with In and Ga as well as with S, Se, and Te [e.g., $Cu(In,Ga)Se_2$]. The bandgap and the corresponding energy levels can be adjusted according to the requirements of an optimized heterojunction through the composition of the solid solution. Whereas lattice matching is an important prerequisite for low defect concentrations in III-V compounds, the chalcogenide II-VI and I-III-VI_2 compounds are
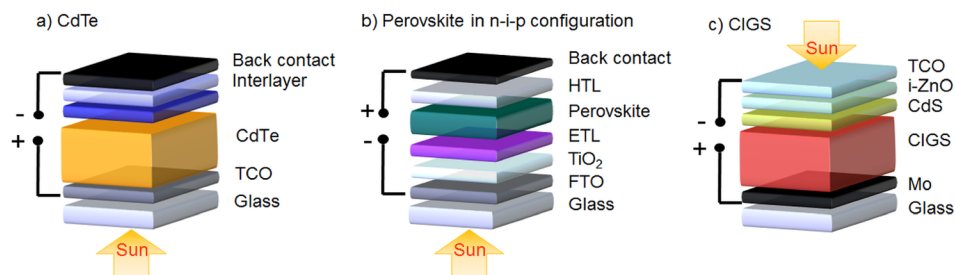
FIG. 1. (a) Superstrate configuration for CdTe cells and for (b) perovskite cells in the n-i-p configuration and (c) substrate CIGS cell configuration.

amazingly tolerant even at strong gradients of the lattice constants despite the likelihood of structural defects. The PSC material system is still in the initial stage of exploration. Here, composition variations also enable tuning of the bandgap, band alignment, doping, and phase stability.

Engineering of the alloys allows the creation of efficient heterostructures and graded barrier layers, e.g., to form selective contacts with low recombination losses. Such strategies include forming a barrier for minority charge carriers which reduces recombination losses at the ohmic back contact and increasing the bandgap at the heterointerface of the junction to increase the built-in voltage. Furthermore, introducing drift fields could improve carrier collection. The recent progress and current status of the performance of thin-film solar cells are visualized in Fig. 2.

Regarding the commercial status of these thin-film photovoltaic technologies, CdTe and CIGS are being produced on a large scale. In 2017, approximately 4 GW of thin-film modules were shipped, corresponding to roughly 4% of all modules.[2,3] The market share of CdTe is about three times that of CIGS. New thin-film production lines are in the construction phase and due to go online in the near future, and so, the market for thin-film PV is expected to grow in step with the entire PV market. In the future, the thin-film technologies should profit from their largely untapped potential for cost reduction as production capacity increases. The cost-reduction potential involves integrated production lines which combine large-area and low-cost processes with high efficiency and low energy consumption.

This article will focus on the materials developments for thin-film PV. When considering the commercial product, it is also necessary to address the lifetime and long-term stability of the modules. The reputation of thin-film solar cells with respect to stability was hampered by the early developments, e.g., Cu_2S-based solar cells in the 1970s. However,

the materials of modern thin-film solar cells have proven their long-term stability in the field. CdTe and CIGS are thermodynamically stable under operating conditions.[4,5] In fact, metastabilities that can be observed under certain operation conditions as well as under light and forward bias tend to lead to improved performance. The stability of perovskite-based cells is a major research topic, and improvements are constantly being reported in the literature.[6] Research and testing are ongoing to provide reliable information to investors and manufacturers regarding the expected performance over the lifetime of the modules in the field.

II. CdTe-BASED MODULES: THE COMMERCIAL BENCHMARK

A. Material characteristics and device concepts

CdTe is one of the first materials investigated for solar cell applications from early on. CdTe has nearly ideal properties for PV cells and modules. It has a direct bandgap of 1.5 eV, which is very close to the optimum for solar energy conversion according to Shockley-Queisser,[7] as well as sufficient charge carrier lifetime and mobility as prerequisites for high-efficiency devices. After a first successful demonstration, it took quite a while until the performance expected from the materials properties was reached. A quite comprehensive review describes the progress of CdTe since the 1950s.[8]

There are several advantageous features of CdTe for solar cell applications:

- the intrinsic advantages of thin-film technologies for large-area photovoltaic modules as also discussed elsewhere in this article
- the nearly ideal bandgap of 1.5 eV
- its tolerance to electronic defects with easily controlled recombination properties
- easy control of film properties during thin-film deposition
- synthesis of high-quality films even at moderate substrate temperatures below 600 °C.

Drawbacks of the CdTe-based modules on a large production scale are a possible limitation of Te supply due to the scarce abundance and environmental concerns.[9]

Several features of the material are particularly favorable for industrial manufacturing. High-quality semiconducting films can be deposited at moderate substrate temperatures. Congruent evaporation and condensation facilitate the control of composition. This means that the stoichiometric composition is relatively simple to achieve since the components Cd and Te each have a higher vapor pressure than the final compound CdTe. As a result, excess of one component will
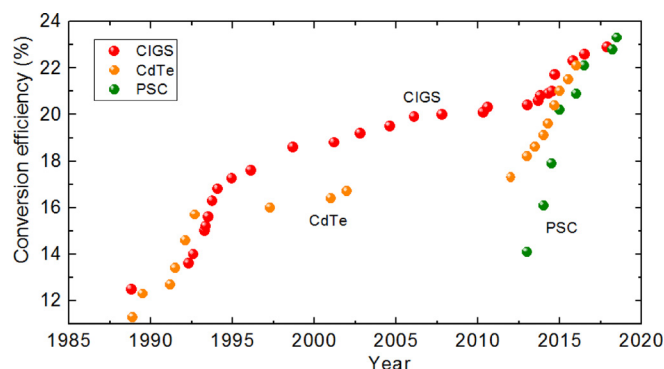

FIG. 2. Record efficiencies of thin-film solar cells CIGS, CdTe, and PSC since 1987. Plotted using data available online collected by NREL, see Ref. 1.

always re-evaporate, leaving behind the stoichiometric composition. These advantageous properties allow a variety of thin-film deposition methods such as evaporation, sputtering, electrodeposition, and others.[8] Currently, evaporation is standard, and this method is applied on a gigawatt scale by First Solar.[10] Figure 3 illustrates two common evaporation techniques for the thin-film deposition of CdTe: close space sublimation and vapor transport deposition. Both methods involve evaporating the CdTe compound and its condensation on a slightly cooler substrate. For close space sublimation, both the source and the substrate are in the same chamber and the substrate is over the source (bottom-up evaporation). The vapor transport deposition process uses a carrier gas to transport the vapor from the source to the substrate, thus enabling a top-down configuration which has some advantages for the mechanical requirements on the substrate and its movement through the deposition machine.

For a long time, the structure of the CdTe solar cell was based on SnO_2-coated glass with a CdS window layer and a CdTe absorber. Significant efforts were put into the development of a stable ohmic back contact on the p-type CdTe. The efficiency was limited to about 16% for laboratory-based cells. Main losses were due to the parasitic absorption in the CdS window layer and a significant deficit of the open-circuit voltage of 0.6–0.8 V. The breakthrough to the expected high efficiency and key advancements within the last decade were a result of detailed loss analysis with respect to current generation and collection, also improving open-circuit voltage and fill factor.[11] Learning from the developments which led to improvements in other state-of-the-art solar cell technologies, like, e.g., employing composition gradients, the CdTe technology could also achieve improved control of doping, as well as reduced recombination at contacts and interfaces.[11] In-depth analysis of material, interface, and device properties shows that by choosing the appropriate material combination

and preparation techniques, efficiencies beyond 25% can be reached with polycrystalline thin-film solar cells.[12]

In recent times, basic material properties have improved by a better control of impurities and doping. For example, Cu was commonly used as a dopant to increase the p-type carrier concentration. However, Cu doping has now been identified as a source of defects and instabilities.[13,14] Efficient doping is obtained by employing the group V elements P and As. The generally applied activation step of the absorber layer by a $CdCl_2$ treatment is also a subject of experimental research with the goal of finding a replacement that can be more easily handled in a production environment.[15]

Even though the bandgap of CdTe is close to the optimum for solar energy conversion, the efficiency was limited by the open-circuit voltage for a long time. An important step forward was to reduce the voltage deficit.[16] The potential of the material has been recently demonstrated in ideal structures with highly crystalline materials, either bulk single crystals or epitaxial films.[17,18]

The II-VI compounds can form alloys either by mixing anions or cations. Table I shows an overview of the bandgaps (E_g) in the alloy system.

Earlier attempts with the (Zn,Cd)Te alloy did not lead to improved devices. Anion alloying exhibits significant bowing of the dependence of the bandgap on the Te/Se or Te/S ratio, with the lowest bandgap in-between the endpoints. This reduced bandgap results in higher photocurrents. The Cd(Se,Te) alloy has low defect densities even when strong gradients are introduced. This finding is in contrast to the originally used CdS/CdTe heterostructures where performance was limited by defects in the interdiffusion region between these compounds.

Tailoring the band structure in thin-film cells by appropriate alloying started with CdS-CdTe. Recent breakthroughs in efficiency were achieved using the Cd(Se,Te) alloy system.[19,20] Appropriate grading of the absorber provides improvements to both the open-circuit voltage and the photocurrent. On the one hand, the bandgap is reduced due to the bowing, leading to an extension of the absorption to lower wavelength. On the other hand, the intrinsically n-type CdSe provides a good heterojunction.[21] Cd(Se,Te) might even have lower grain boundary (GB) recombination velocity as compared to the binary compound CdTe. In a CdSe-CdTe heterojunction, a good blue response is still obtained even though the n-type side has a low bandgap of only 1.7 eV. The good quality of the material and remarkably good transport properties found in Cd(Se,Te) allows current collection also from the n-type side of the heterojunction. Recombination

CdTe Deposition

a) Close space sublimation
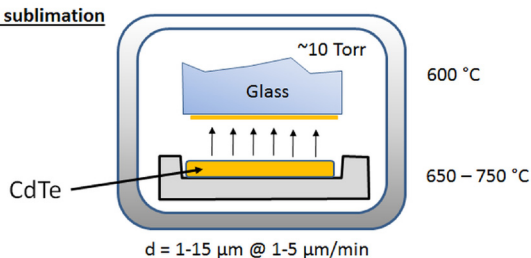
b) Vapor transport deposition
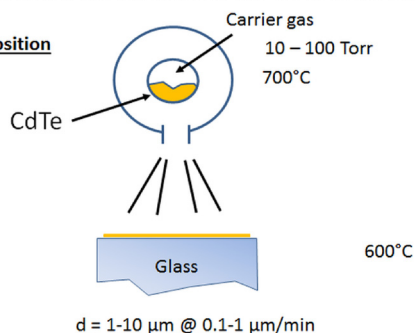
FIG. 3. Preparation methods for CdTe deposition. (a) Close space sublimation and (b) vapor transport deposition.

TABLE I. Bandgaps of II-VI compounds applied in CdTe-based solar cells.

Alloy system	Low E_g (eV)	High E_g (eV)	Minimum E_g
(Zn,Cd)Te	1.5	2.26	
Zn(Se,Te)	2.26	2.7	2.1
Cd(Se,Te)	1.5	1.7	1.32
Cd(S,Se)	1.7	2.4	
Cd(S,Te)	1.5	2.4	
(Mg,Cd)Te	1.5	3.2	

TABLE II. Materials for contacts and doping of CdTe solar cells.

Back contact	Absorber/doping	Heterojunction buffer layers	Comment
CuTe	Cu		Cu should be avoided
C	P	a-Si	
ZnTe	As	(Mg,Cd)Te	
Te	$CdCl_2$/$MgCl_2$	(Zn,Mn)O	

velocities of less than $100\,cm/s$ at polycrystalline Al_2O_3/ CdS(Se,Te) interfaces demonstrate the favorable electronic properties of the alloy.[22] Further optimization of the absorber is obtained by increasing the p-type doping of the absorber. Since Cu has been found to also be a lifetime killer, group V elements are now favored for this purpose.

Further improvements in the device efficiency are due to optimization of contacts, by modifying both the heterojunction and the contact.

Table II lists the materials used in the development of efficient and stable devices.

Besides the good tolerance with respect to defects, the charge carrier recombination at grain boundaries and interfaces appears to be controllable by the proper choice of the passivation layer. The wide range of options for materials optimization was demonstrated by exploring various combinations for passivation and contact interfaces. The flexibility of the material combinations revealing the significant potential of the material for even higher efficiencies is demonstrated in a recent work also using a-Si as a p-type contact.[23] The lifetime was found to increase typically to more than $100\,ns$ as measured by photoluminescence (PL) decay. Extremely low recombination at CdTe/(Mg,Cd)Te heterointerfaces has also been shown.[24] Passivation by Al_2O_3 leads to recombination velocities of less than $100\,cm/s$.[22] The recombination with suitable window layers (Zn,Mg)O and a (Mg,Cd)Te buffer led to efficiencies around 20%.[23]

Other improvements are related to the back contact. For a long time, Cu-containing compounds were applied in order to obtain a good ohmic contact (e.g., copper-filled graphite). By optimizing alloys with ZnTe, control of back contact stability is obtained. Furthermore, this contact can be made to selectively conduct holes.

Recent developments also benefitted from sophisticated measurement techniques like lifetime tomography[25] which can allocate the effect of $CdCl_2$ treatments on a microscopic scale. Applying space-, wavelength-, and time-resolved spectroscopic methods reveals problems of doping segregation and grain boundary recombination. However, the interpretation of these results must consider the entire device structure. Internal fields and potential barriers may negatively influence solar cell performance.

B. Module aspects and solar cell and module performance

CdTe modules are produced using monolithic integration techniques analogue to those described in detail for the CIGS technology in Sec. III E. Table III displays some selected data of laboratory cell and module performance.

TABLE III. Selected data of CdTe record laboratory cells and modules.

Cell/module	Area (cm^2)	V_{oc} (V)	j_{sc} (mA/cm^2)	FF (%)	Eff. (%)
Cd(Se,Te) cell	0.4798	0.8872	31.69	78.5	22.1[26]
CdTe x-tal	0.2	1.017	21.7	61.7	13.6
Module	7038.8	110.6	1.533	74.2	18.6[26]

The efficiency of 22.1% in the laboratory demonstrates the competitive performance level to be expected for future module developments.

The CdTe module market is clearly dominated by the American company First Solar which has increased the module size to $2.0 \times 1.2\,m^2$ with a nominal power of 440 Wp for the latest manufacturing generation. They have already sold over 17 GW of modules worldwide. Its main market is large-area, utility-scale power plants. Recent developments include increasing the product size by more than three times from $0.72\,m^2$ to $2.4\,m^2$. The larger size has cost advantages for manufacturing and installation which translate to lower overall costs for electricity generation. Connecting approximately 9×10^6 of the former 80-W-sized panels, one of the largest power plants "Topaz Farm" with 550 MWp was built in California USA from 2001 to 2014.[27] Figure 4 shows the satellite image of this large installation from Google Earth.

Stability was once an issue due to the loss of p-type carrier concentration and stability of the back contact.[28] In the meantime, the stability and long-term performance of First Solar CdTe modules have been proven over a long testing period in practical operation and at specific test sites. The modules show very good stability and high performance ratios.[29] Another stability issue is related to partial shading, which is an issue for all PV modules but mitigated for Si technology by integration of bypass diodes. As also described for the CIGS technology in Sec. III E along with a mitigation strategy for thin-film modules, partial shading of the module—meaning that individual cells or groups of cells are generating significantly less current than the remainder

FIG. 4. Satellite image of the utility-scale installation "Topaz Farm" with 550 MWp of CdTe-based thin-film modules manufactured by First Solar in Arizona, USA. Imagery and Map data from Google.

of the module—can lead to localized areas of reverse bias and potentially damage the module. Solar installers and users should be aware of inappropriate mounting or cleaning procedures to avoid.

An important discussion regarding the possible production scale, e.g., up to terawatts, for CdTe modules centers on the limited availability of Te. Considering all aspects of recycling and market dynamics,[30] the limit for accumulated installations up until 2050 was calculated to about 2 TWp. This calculation indicates that a significant share on the market is possible before Te availability plays a cost-driving role. Regarding environmental concerns, a holistic evaluation of the technologies published by Sinha and Wade claims that the environmental footprint for CdTe is the smallest among all PV technologies.[9]

III. CIGS-BASED SOLAR CELLS, THE PATH TO VERY HIGH EFFICIENCIES

In Secs. III A–III E, we will concentrate on the $Cu(In,Ga)(S,Se)_2$ (CIGS)-based thin-film solar cell technology. First, basic properties of the CIGS material and important aspects of the phase diagram will be discussed along with the basic device design considerations. Then, we will highlight the specific aspects related to achieving the highest efficiencies with the CIGS material system, followed by a description of the current production-relevant processing methods and module designs. Table IV, consisting of CIGS module manufacturers and their processing options, concludes the chapter.

A. Basics of CIGS materials

The CIGS photovoltaic technology is named after the compound semiconductor in which the sunlight is absorbed—the so-called absorber layer. CIGS is short for $Cu(In,Ga)(S,Se)_2$, which has the chalcopyrite crystal structure. The parentheses indicate that the enclosed elements are interchangeable on the I-III-VI$_2$ lattice. Further combinations are possible and have also been investigated, e.g., exchanging Cu by Ag or including Al with the mixture of In and Ga. Even Te has been added to the chalcogen mix of S and Se (O behaves differently). As a solid solution, the chalcopyrite crystal structure retains the tetrahedral bonding, but the bond lengths vary with the alternative element, which results in shifted lattice constants and therefore also changes the bandgap of the semiconductor, as illustrated in Fig. 5. Bandgap modifications are possible with minimal lattice strain if both cation and anion species are properly adjusted. The system is generally found to follow Vegard's law corrected by a bowing parameter.

The bandgap of the CIGS layer is therefore determined by its composition and is not necessarily uniform in or through the film. In fact, a composition gradient between the front and back contacts is found to be desirable in order to achieve high conversion efficiencies, as will be discussed later. At the same time, lateral uniformity across the area of the cell is desirable for highest efficiencies.

The growth of these polycrystalline films in industrial processes is covered in more detail in the following. We distinguish between the sequential or two-step process and the coevaporation process, illustrated in Fig. 6. All methods involve a reaction of the metals Cu, In, and Ga with Se and/or S to form the near-stoichiometric chalcopyrite α phase $Cu(In,Ga)Se_2$ because the unmodified compound would dissociate upon evaporation in a high vacuum. The selenium supply must be higher than that required for stoichiometry for good quality films. It has also been shown that the final copper content needs to be slightly less than 25 at. % because of the ready formation of $Cu_{2-x}Se$—the presence of which causes shunting in the photovoltaic cell.

In the so-called **sequential process**, the CIGS compound is formed in two steps. Cu, In, and Ga precursor layers are deposited onto the substrate in the required amount. Evaporation, electrodeposition, or even inks could be used as the coating method for this step. However, sputtering has proven to be the most successful and widely used method for production, profiting from previous experience in the glass-coating industry in scaling-up the coating process in the flat-panel display industry. Typically, pure In targets are used. Ga is incorporated into the Cu target since pure Ga has a very low melting temperature below 30 °C. Defined sequences of the precursor layer stacks can influence the distribution of the elements through the depth of the final film. Sometimes, the precursor layer will already incorporate some Se.

This precursor layer is then annealed and selenized in an atmosphere of elemental Se or in H_2Se or sulfurized using S or H_2S, or both. A process established by Solar Frontier employs sulfurization after selenization (SAS). The resulting CIGS layers have an enrichment of Ga towards the back contact, as is typically found for many sequential processes.[31] This Ga gradient is a result of the slower reaction kinetics of Ga as compared to In. The sulfurization step increases the sulfur content towards the film's surface. This combination leads to a beneficial double grading in the bandgap profile.[32] Such a profile can be desirable for high efficiencies by reducing recombination at the CIGS/Mo or CIGS/buffer interfaces. If time for heating-up and cooling-down is also considered, the whole process can last several hours which is why a number of substrates are treated at the same time in a batch process.[33] Exact process conditions and speeds are kept confidential by companies.

Instead of using a chalcogen atmosphere, it is also possible to use a so-called stacked-elemental layer (SEL) process. Here, Se is deposited on top of the sputtered precursor layers and the whole stack is then subjected to a rapid thermal processing (RTP) step, which might even be in a S-containing atmosphere.[34] This process also results in a composition gradient with increased Ga towards the back contact and, if provided, increased S towards the front surface, resulting in a double-grading of the CIGS absorber bandgap.

The complex phase formation process in sequential processes has been widely studied in the past, with detailed information obtained by time-resolved *in-situ* XRD experiments.[32,35,36] In order to obtain high-quality CIGS films over a large area with uniform properties, like composition and elemental depth profile, morphology, and crystallographic phases, it is indispensable to control gas concentrations,

TABLE IV. Overview of current CIGS module producers. AZO: Al-doped Zinc Oxide, CBD: Chemical bath deposition, ITO: Indium Tin Oxide, MOCVD: Metal-Organic Chemical Vapor Deposition, Monol.: monolithic interconnection, PVD: Physical Vapor Deposition, SLG: Soda-Lime Glass, sputt.: sputtering, R2S: Roll-to-Sheet, R2R: Roll-to-Roll, RTP: Rapid Thermal Processing, ap: aperture area, and tot: total area.

Company (country)	Substrate, handling	Substrate size (L × W [cm²])	CIGS process	Buffer (process)	TCO (process)	Cell interconnection	η (area [cm²]) best reported modules	Production capacity [MW] (country) actual	Production capacity [MW] (country) planned	References
Ascent Solar Technologies, Inc. (US)	Polyimide, R2R		Coevaporation			Monol., grid-assisted (laser and precision screen printing)	11.9%ap[b] 9.8%ap[b] (970)	30		Ascentsolar.com
Avancis GmbH (DE)	SLG, with a higher strain point, with a SiN Barrier	159 × 66	Sequential, stacked elemental layer process (SEL): Cu-In-Ga:Na (sputt.), Se (therm. evap.) on top; RTP in S-containing gas	In$_x$S$_y$:Na (PVD)	AZO (sputt.)	Monol. (laser and scribing)	18.2%[b] (900)	100 (D) 100 (KR)	100 (D) 100 (KR) 1500 (CN)	34,116
Eterbright Solar Corporation (TW)	SLG	190 × 124		ZnS$_x$		Monol.	15.4%tot[b] (23 500)			Hulket.com
Flisom AG (CH)	Polyimide (up to 100 cm width), R2R	310 × 41	Coevaporation			Monol. (laser), foil cutting, and sub-module sorting and contacting	8.4%tot[b] (3588) 9.0%tot[b] (6646) 9.4%tot[b] (12 762)	15		Flisom.com
Global Solar Energy, Inc. (US)	Stainless steel foil (up up to 49 cm width), R2R	up to 570 × 49	Coevaporation bottom-up	CdS	ITO	Laminating flexible cells to a polymer with patterned metallic conductors (integrated cell interconnect ICI)	12.7%ap[b] (7900) 16.3%ap[b] (3921) 16.7%ap[b] (971)	50	300	135,136
Group Solar Hong Kong GSHK (CN)	Stainless steel foil, R2R	260 × 100	Coevaporation bottom-up		(sputt.)	Laminating flexible cells to a polymer with patterned metallic conductors (Integrated cell interconnect ICI)	16.5%ap[b] (26000)	>100		137
Jennfeng (TW)	SLG	141 × 111				Monol	8.3%tot[b] (15 600)			Jennfeng.com
Mia Solé Hi-Tech Corp. (US)	Stainless steel foil, R2S	up to 260 × 99	Sputtering and reactive sputtering	CdS (sputt.)	(sputt.)	Cell stripes, low resistance collection grid, and Ultrawire (TM) interconnect	16.6%[b] (25 788) 17.9%ap[b] (4900)	100	900	114,117,136,138
Midsummer AB (SE)[a]	Punched stainless steel substrates (156 × 156 mm²) with a conductive diffusion barrier		Sputtering of multiple layers from compound targets at 550 °C	In$_2$S$_3$ (sputt.)	ITO based TCO bilayer (sputt.)	Stringing of cells, like in silicon panels				109,113,132
NICE Solar Energy (D/CN)	SLG	120 × 60	Coevaporation Top-down	CdS (CBD)	AZO (sputt.)	Monol. (laser and scribing)	16.0%tot[c] (7200)		350	112,126
Shandong Sunvim	SLG		Sequential, Se on			Monol.	10%[b] (6000)	30		136

TABLE IV. (Continued.)

Company (country)	Substrate, handling	Substrate size (L × W [cm²])	CIGS process	Cell interconnection	Buffer (process)	TCO (process)	η (area [cm²]) best reported modules	Production capacity [MW] (country) actual	Production capacity [MW] (country) planned	References
Solar Technology Co. Ltd (CN)			top of precursor and RTP process							
Solar Frontier KK(JP)	SLG	126 × 98	Sulfurization after Selenization (SAS) Process	Monol. (laser and scribing)	Zn(S,O;OH)$_x$ (CBD)	ZnO:B (MOCVD)	19.8%ap[c] (35) / 19.2%ap[c] (900)	1110		125,139–141
Solibro GmbH (DE)	SLG		Coevaporation bottom-up	Monol. (laser and scribing), Grid assisted	CdS (CBD)	AZO (sputt.)	17.5%ap[c] (9395) / 18.7%ap[b] (900)	145	300	136,142,143
Sunshine PV Cooperation (TW)	SLG	140 × 110	Sequential	Monol. (laser)	CdS (CBD)	ITO (sputt.)	9.7%tot[b] (15400)	30	45	136

[a]Not a producer itself, but has supplied several production lines.
[b]In-house measurement.
[c]Certified measurement.
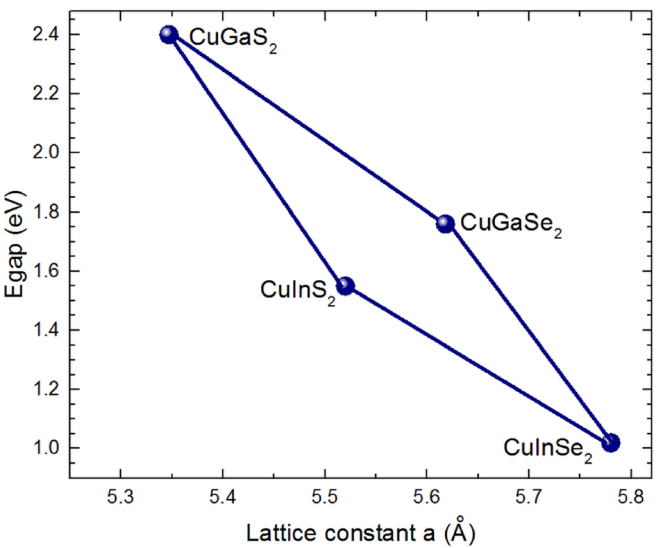

FIG. 5. Correlation between the bandgap and lattice constant a as a function of composition in Cu(In,Ga)(S,Se)$_2$ solid solutions.

distributions, pressure, and temperature during the entire selenization process and across the whole substrate size. Despite these challenges, Solar Frontier successfully mass-produces commercial CIGS solar modules.

In the **coevaporation** processes, the constituent elements Cu, Ga, In, and Se are thermally evaporated simultaneously in a high vacuum system where they condense onto a heated substrate. While the final integral composition for all high-quality CIGS modules typically has a GGI = [Ga]/([Ga] + [In]) ratio of 0.30–0.35 and Cu contents of 20–22 at. %, there are different options on how to reach this final composition. The simplest option is the single-stage process with the coevaporation sources supplying the correct amount of material for the growth of slightly Cu-poor CIGS throughout the film deposition time. This material has a rather small grain size. Cu-rich materials would have large grains but would also contain the conductive Cu$_{2-x}$Se phase and short-circuit the solar cell. Single-stage CIGS generally has no composition gradient unless
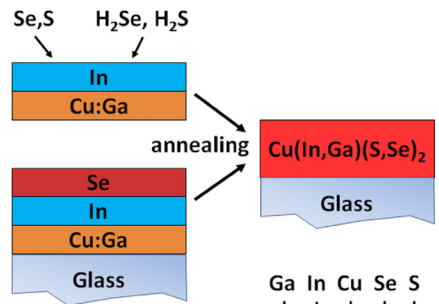
FIG. 6. CIGS deposition methods: sequential processes or coevaporation of the elements.

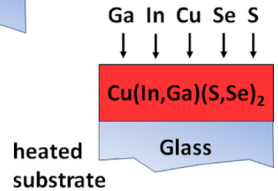the Ga and In rates were changed during film growth. The two-stage or bi-layer process is often termed the Boeing process[37] after the Boeing aerospace company first employing it. It involves growing the CIGS with an initial Cu-rich composition in order to obtain large grain sizes and then to reduce the Cu supply while maintaining the rates of the other elements until an overall Cu-poor composition, as required for high efficiencies, is obtained.

In the three-stage process, as first proposed by Gabor *et al.*,[38] a Cu-free film of $(In,Ga)_2Se_3$ is initially deposited, then transformed by coevaporation of Cu and Se into Cu-rich CIGS with excess Cu-Se forming on top, and finally converted in the rather short third stage into device-grade Cu-poor CIGS by again supplying only In, Ga, and Se. This process enables tuning of the double grading of the bandgap profile[39] by changing the ratio of Ga to In and the thickness of stage one and stage three, respectively. By starting with a Cu-poor CIGS instead of Cu-free CIGS, a modification known as the CUPRO process ("Cu–poor-rich-off") can be performed.[40]

Besides $Cu_{2-x}Se$, which forms for Cu contents near or above the stoichiometric value, another important player in the CIGS phase diagram is a Cu-poor variant generally present on the surface. This variant is known as the "ordered defect compound" (ODC) and has an elemental composition of roughly $Cu(In,Ga)_3Se_5$. For higher Ga and/or S contents, a $Cu(In,Ga)_5Se_8$ surface composition is found. The presence of alkali elements like sodium and potassium during film growth have been found to affect the resulting film composition, crystal structure, grain size, and electronic properties. The latter can be adjusted by treatments with alkali elements after the growth process, see Sec. III C 1.

The $Cu(In,Ga)Se_2$ thin-film layers contain many material defects within the crystallite bulk and at the surface and the grain boundaries. Some are electronically active, and some are apparently not. The defects originate from faults in the crystal structure, like stacking faults, vacancies, and anti-site defects, but also from the presence of additional elements like the alkali elements. It is rather difficult to dope CIGS n-type since the natural defects like Cu and Se vacancies result in p-type doping. For this reason, CIGS is typically paired with the n-type buffer-window layer combination of CdS, non-doped ZnO, and Al-doped ZnO. As a heterojunction, defects will be present at the materials interface. Furthermore, compositional gradients will also generally induce defects related to lattice strain.

The thin polycrystalline films have typical grain sizes between 50 and 2000 nm, sometimes with a uniform size distribution and sometimes very mixed. These features depend a lot on the specific processing parameters including the properties of the underlying materials (typically Mo and glass). While columnar grains with grain boundaries perpendicular to the plane of the device stack could be advantageous, since the current flow is then not required to cross a grain boundary, also very-high-efficiency devices have been produced with non-uniform grain sizes and grain boundaries perpendicular to the current flow.[41] For this reason, grain boundaries are not considered the limiting factor for increasing device performance at this stage of development.

However, further improvement of crystallinity may be important for absolute highest possible efficiencies.

B. Solar cell device design

1. Substrates

The typical device structure for a CIGS solar cell is shown in Fig. 1(c). It is traditionally prepared in the substrate configuration starting on the metallic back contact.

Both rigid and flexible substrates can be employed for CIGS. The choice of substrate must meet several requirements for the PV module application. It serves as a mechanical support for the very thin active layers and simultaneously as an encapsulating layer at the bottom. Surface roughness has to be smooth enough to allow good coverage of the subsequent layers and to avoid shunting between back and front contacts. Furthermore, the coefficient of thermal expansion (CTE) has to be similar to that of the following layers in order to avoid cracking or adhesion problems. Process conditions like temperature, atmosphere, and chemicals for all the following steps have to be compatible with the substrate and not cause any corrosion or adverse reaction, especially in an aggressive Se atmosphere. Apart from the chemical and mechanical stabilities, possible diffusion of detrimental elements into the device also has to be avoided.

The most widely used rigid substrate is standard flat soda-lime glass (SLG), like that used for windowpanes, with a typical thickness of 1–3 mm. A glass transition temperature of approx. $570\,^{\circ}C$ limits process temperatures somewhat. At this time, the production capacities for flat SLG exceed by far the capacity needed for PV modules.[42] It is therefore not yet possible to obtain special tailored glass compositions in large amounts for a competitive price. There are reports on the beneficial use of specialty glasses in laboratories,[43,44] with the aim of exploiting a higher strain point of the glass by employing higher process temperatures. A big advantage of SLG is that it contains 15%–20% of NaO_2,[45] which is the source of Na which out-diffuses into the CIGS layer during growth and leads to improved properties of the solar cells (see Sec. III C 1). The glass composition, among other factors, determines the mobility of sodium in the glass. As the location of the glass manufacturing, together with the employed material sources, can influence the composition, and also age and storage conditions of the glass can influence the sodium diffusion, it is important for an industrial production line to ensure constant properties of the substrate.[46] One option to reduce the dependence on the sodium supply from the glass is to use a barrier layer and to provide an external supply of sodium, e.g., via a doping layer of sodium fluoride or sodium-doped molybdenum back contacts.

Flexible substrates have several distinct advantages, such as lower weight, besides being able to bend them. They are thus attractive for specific markets like in consumer products or BIPV, enabling their use on less-stable flat roofs or on curved facades. Moreover, the production in roll-to-roll or roll-to-sheet processes offers new possibilities and potentially lower production costs. A good review dedicated to flexible substrates can be found in Ref. 47. Metallic foils and polymers are the two types of flexible substrates for which

processes and machines have been developed up to the production scale.

Polymers are suitable flexible substrates for CIGS solar cells and modules. Specifically, polyimide (PI) is an attractive choice due to its vacuum and temperature stability. Typically, foil thicknesses of about 20–30 μm are employed. It is electrically insulating like SLG, which allows the application of the same monolithic interconnection scheme for modules. However, they do not supply sodium and require an alternative source just like SLG with a barrier layer. The thermal stability of PI, as well as the CTE of some PIs, limits process temperatures to about 450 °C, which is more than 100 °C less than that typically applied for CIGS on SLG.

Metal substrates like stainless steel or titanium, on the other hand, can withstand temperatures at least as high as those used for SLG. While this is desirable for the growth of the absorber, it is also a challenge to develop suitable barrier layers to avoid the diffusion of detrimental elements from the metal substrate. Specifically, Fe, Cr, and Ni are known to harm the CIGS absorber, even in very small quantities.[48,49] If monolithic interconnection is to be employed, an additional challenge is that the diffusion-blocking layer must also be electrically insulating. However, there are other options for cell interconnection, like, e.g., shingling, which do not have this requirement.

For flexible solar cells and modules, all the additional barrier layers, diffusion blocking layers, or doping layers for alkalis must also be compatible with the processing conditions of the entire device. They must be thin and flexible enough for the intended use in a flexible module and the expected bending radii.

2. Back contact

While other materials have been tested as the back contact for CIGS solar cells,[50] sputtered molybdenum with several 100 nm thickness consistently emerges as the best selection. The CIGS growth process takes place in a highly corrosive Se/S environment in which Mo is rather stable as compared to other options. A thin layer of $MoSe_2$ forming at the Mo/CIGS interface during CIGS growth has been shown to improve adhesion and electrical contact properties with CIGS if it has the right orientation.[51,52] Well-functioning solar cells are even produced with extremely thick $MoSe_2$ layers of 500 nm or larger.[53] The Mo deposition process affects the density of the final film and also the diffusion properties of alkali elements from the glass through Mo to the growing CIGS layer. The supply of alkali elements during CIGS growth can therefore be controlled by means of the Mo processing parameters. An amorphous phase can be detected in-between the columnar Mo grains, consisting of a mixture of MoO_3 and Na_2MoO_4. This result clearly indicates the presence of sodium[54] in the Mo layer and how the grain structure provides transport channels for the sodium from the glass.

Stress and Na content of the Mo films can be tuned via the sputter conditions, mainly via pressure.[55] Another option to incorporate Na, if it is not provided by the substrate, is to use a Na-doped Mo-sublayer, which can also be prepared by sputtering.[56]

3. Heterojunction formation

The CIGS layer itself is the p-type absorber layer with a suitable bandgap which is combined with an n-type front contact to form a p-n heterojunction. The photons which are absorbed in this layer generate free charge carriers that can be collected as photocurrent in the solar cell. Like for all solar cells, the criteria for absorption are that the photons arrive through the window layer, that they have a higher energy than the bandgap, and that the film is thick enough according to the absorption coefficient. Since the local bandgap depends on the local composition, an efficiency-enhancing profile can be engineered to maximize both current generation and voltage.

Figure 7 illustrates the double-graded bandgap profile frequently employed for high-efficiency CIGS solar cells in order to attain an increased E_g towards both the junction and the back contact sides of the film. The slope with increasing E_g towards the back contact reduces the concentration of electrons available for recombination at that interface. Towards the front contact, a larger bandgap is desirable within limits, as it will generally lead to a higher built-in diode voltage and thus higher open-circuit voltages. However, the charge carrier transport can also be disturbed or a higher concentration of defects is generated if the bandgap or the slope is too extreme. In order to absorb and convert photons with lower energies, a minimum E_g is implemented near the junction side, resulting in an increased photocurrent. We refer to this minimum E_g as the "optical bandgap" since it is the value found when measuring the absorption edge. Within a certain range, the double-grading scheme enables higher conversion efficiencies than those which would be possible in a device with an absorber layer of homogeneous composition.[57] The bandgap grading is typically realized through the variation of the gallium content in the multi-stage coevaporation process or by sulfurizing the surface after a selenization process (which naturally provides a GGI gradient with increased Ga towards the back contact due to the lower reactivity kinetics of Ga as compared to In). Exchange of Cu by Ag increases E_g slightly, and exchange of In by Al causes a large increase in E_g.

4. Buffer layer

Historically, CdS was employed as a thick layer of evaporated n-type semiconductor forming the heterojunction with
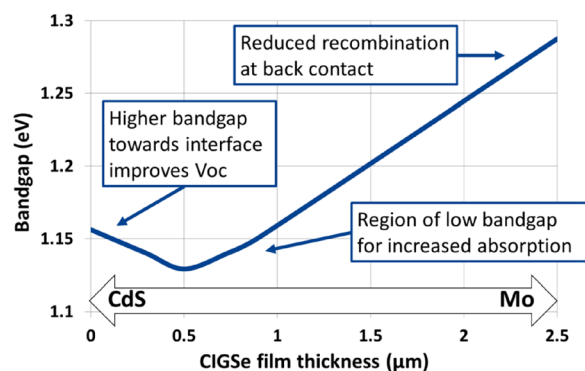

FIG. 7. Double-graded bandgap profile in CIGS with labels to indicate how its features influence the solar cell performance.

co-evaporated Cu-Se, which was later exchanged with CuInSe$_2$ since the CdS/CuSe combination was not sufficiently stable. The CdS bandgap of only 2.4 eV, however, leads to absorption losses. Experiments with ZnO-based n-type layers only led to acceptable device performance if a thin layer of several tens of nanometers of CdS, the so-called buffer layer, was included, resulting in the typical CIGS solar cell stack commonly used today. This very thin CdS layer is now typically deposited in a chemical bath deposition (CBD) process which results in very thin and conformal coatings, as illustrated by the scanning electron microscopy image of a CIGS/CdS cross-section in Fig. 8. The role of the thin CdS layer is still being discussed, but is generally understood as somehow passivating the CIGS surface, while also providing proper band alignment between CIGS and the window layer as well as providing n-type charge carriers for the pn-junction formation.[58] It is also thought to protect the CIGS interface from sputter damage from the subsequent processing steps. However, it must be remarked here that some groups have reported efficient buffer-free devices.[59]

CdS is still used very successfully for CIGS solar cells, and the highest efficiencies are reported with CdS buffer layers. It leads to a uniform coverage even for very thin layers and rough or steep topography and has an *in-situ* cleaning effect.[60] An alkaline aqueous solution containing a Cd-salt, ammonia as a complexing agent, and a sulfur source like thiourea at a typical temperature of 60 °C is used. Different process recipes have been developed and improved with respect to the deposition rate and material utilization.[61] One disadvantage is its rather low bandgap of only 2.4 eV, meaning that even a typical very thin layer of 50 nm still absorbs a considerable amount of light, which then does not contribute to the photocurrent. Therefore, alternative higher bandgap materials are desirable. At the same time, a Cd-free layer would be advantageous with respect to environmental aspects. Hence, different materials and techniques besides CBD-CdS have been used for the buffer layer, see, e.g., the reviews.[65,66]

Sputtering has also been studied intensively as a preparation technique because this dry technique is much more compatible with vacuum deposition processes.[62,63] Further options like ALD or ILGAR[64] have shown promising results

but have not yet been implemented in a production line. Additionally, there is research towards avoiding the buffer layer completely, recently leading to cells of 16.5% efficiency using all dry deposition processes.[59]

Recently, modification of the CIGS surface by an alkali post-deposition treatment prior to the buffer deposition has led to significant improvement of the efficiency. This modification will be discussed in more detail in Sec. III C 1.

5. Transparent front contact/window layer

The n-type front contact, the so-called window layer, is completed with a highly conducting and transparent layer, with a sufficiently high bandgap and appropriate band alignment. Among the possible materials which fulfil these conditions,[67,68] transparent conductive oxides (TCOs) have proven to be particularly successful and are widely used. Typically, a bilayer is used which consists of a thin insulating layer, e.g., intrinsic ZnO, which provides some shunt protection for local physical defects like pinholes and serves as a protective layer for the processing of the conductive layer on top, e.g., to reduce sputter damage.

The window layer has to be tuned to the best trade-off between conductivity and transparency. Higher conductivity for lower series resistance and thus higher fill factor in the module can be achieved by using thicker films or a higher doping level with higher carrier density. A thicker film or a higher number of free carriers will on the other hand lead to a reduced transmittance and thus lower photocurrent in the module. The optimum window properties of a module depend additionally on the interconnection scheme, see Sec. III E.

C. Recent developments: Getting close to the theoretical maximum efficiency

With the highest efficiencies for CIGS solar cells approaching 23%, the question arises of how close they can approach the maximum theoretical efficiency and what must be done to get there. Within the CIGS technology, a further increase in efficiency can be realized by optimization of:

- alkali content in the CIGS layer
- charge carrier collection in the absorber layer
- buffer layer

In the following, we will summarize these different strategies in detail.

1. Optimization of the alkali content by alkali fluoride post-deposition treatments

The positive effect of the alkali element sodium on the performance of Cu(In,Ga)Se$_2$ (CIGS) solar cells was first detected in 1993 by comparing CIGS solar cells grown on different glass substrates.[69] The main electrical parameters which are improved by the presence of Na are the open-circuit voltage, V_{oc}, and the fill factor, FF.[70] The increase in V_{oc} is caused by an increase in the net acceptor concentration.[71] There is still an ongoing scientific debate about whether the positive effect of sodium is due to the passivation of defects at grain boundaries (GBs)[72,73] or due to

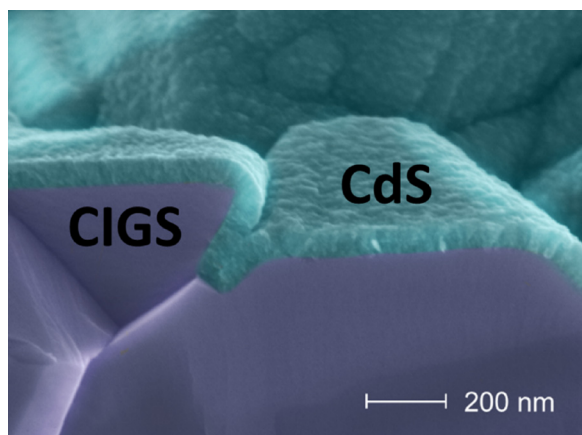
FIG. 8. SEM cross-sectional image of the CIGS-CdS heterointerface.

bulk-related effects.[74,75] It has only recently become possible to locate Na within the CIGS film with high sensitivity. Atom probe tomography (APT) measurements detected Na in the grain bulk up to a concentration of 60 ppm[76] along with a clear segregation of Na at the grain boundaries up to a concentration of 1.7 at. %.[76] Hence, Na is located both inside the grains and at the grain boundaries. Its positive effect can therefore be from either or both locations.

The effect of the heavier alkali elements potassium and cesium on cell performance and CIGS layer properties was also formerly investigated but was not found to be as relevant as that of sodium[77] and then not tested further. In 2012, potassium was re-discovered as an efficiency-boosting player: CIGS solar cells on potassium-containing enameled steel substrates showed even higher cell efficiencies than cells on standard soda-lime glass (SLG) substrates.[78] One effect of K was the higher net charge carrier concentration caused by the additional K doping.[78]

These last results refer to the effect of alkali elements sourced from the substrate, i.e., which are present during and influence the growth of the CIGS layer.[78] To be able to supply alkali elements independently from the substrate without influencing or disturbing the growth of the CIGS layer by the alkali element, a post-deposition treatment (PDT) with alkali-fluoride after the CIGS growth was developed.[79] This PDT for Na is a well-known process for CIGS solar cells on alternative substrates like steel or polyimide foil which do not provide Na like SLG does.[79] In 2013, Laemmle *et al.*[80] have shown that a potassium fluoride post-deposition treatment (KF-PDT)[80] is as efficient to increase cell efficiency as a sodium fluoride PDT.[79] Now, it was possible to supply K to the CIGS layer independently from the substrate. Parallel in time and independently from the work of Laemmle *et al.*[80] at ZSW, Chirila *et al.*[81] also developed a KF-PDT at EMPA, applied it after a NaF-PDT, and thereby increased cell efficiency up to an impressive 20.4% on the polyimide substrate. This value remains the highest efficiency for a thin-film solar cell on a flexible substrate to this day. The initial application of the KF-PDT to CIGS layers grown on glass substrates led to a boost in cell efficiency up to 20.8%,[82] 21.0%,[83] and 22.3%.[84] The KF-PDT worked also well on a sulfur containing absorber based on $Cu(In,Ga)(S,Se)_2$.[84] This trend in the increase in cell efficiency was then continued by the application of the PDT process with the heavier alkali elements rubidium (Rb) and cesium (Cs),[85,86] which then led to an increase in efficiency up to 22.6% by a RbF-PDT. Solar Frontier[87] has since achieved a record efficiency of 22.9% by the application of a CsF-PDT to a $Cu(In,Ga)(Se,S)_2$ layer, which shows that the positive effect of the PDT process also works for sulfur-containing chalcopyrite layers generated by the "sulfurization after selenization" (SAS) process. The PDT could be successfully transferred from the cell level to the module level. Solar frontier demonstrated modules with efficiencies of 19.2% and 19.8% with areas of $30 \times 30 \, cm^2$ and $7 \times 5 \, cm^2$, respectively, by using a KF-PDT on a large area.[88]

The increase in efficiency by the PDT process is caused by different effects: One main effect is a reduced recombination at the absorber buffer interface (which increases V_{oc}) due to a homogenizing effect on the CIGS surface as demonstrated by improved coverage by the CdS layer in the initial growth phase after a RbF-PDT process.[89] This better coverage enables the reduction of the CdS layer thickness without any loss in V_{oc} or FF.[81] The reduced thickness of the CdS layer leads to an enhanced transmission in the UV range to the CIGS absorber layer and hereby to an enhancement in the short-circuit current density.[81] A further observation is that the CIGS surface composition is changed after a PDT process. A strong Cu depletion and K enrichment were observed after a KF-PDT.[81,90] Further, a widening of the surface bandgap to a value of 2.52 eV was measured at the CIGS surface after a KF-PDT.[91] This value corresponds very well to the bandgap of $KInSe_2$ with $E_g = 2.68$ eV.[92,93] Hence, it is proposed that $KInSe_2$ forms at the surface of the CIGS layer during the KF-PDT.[90,94] This bandgap widening, together with a lower surface valence band energy,[91,95] leads to a reduced recombination of charge carriers at the interface to the buffer layer.

Another effect of potassium is an increased free carrier concentration in the bulk of the absorber layer.[78,88] Furthermore, an enhancement of minority carrier lifetime was observed after a KF-PDT.[88] Hence, KF-PDT reduces recombination in the bulk as well as at interfaces.

While most of the results presented above were achieved by applying KF-PDT, several groups have also been experimenting with RbF- and CsF-PDT, which have also enabled very high efficiencies. The enhancement in efficiency with Rb and Cs was more pronounced as compared to KF-PDT.[86] This finding could be explained by the fact that phase separation and formation of an alkali indium selenide compound (like the $KInSe_2$ mentioned above) take place more easily for heavier alkali elements.[96] High-resolution transmission electron microscopy (HRTEM) images of a RbF-PDT CIGS/CdS interface revealed a thin Rb-containing compound[97] which was not observed in Rb-free reference samples. Hence, the modification of the CIGS surface works better for the heavier alkali elements. Further investigations like APT measurements revealed that Rb pushes Na and K away from the grain boundaries and leads to a very strong depletion of Cu at GBs.[98] Hence, holes are better repelled from the GBs by the higher hole barrier at the GBs,[73] leading to lower recombination of electrons, i.e., GBs seem to be better passivated by segregation of Rb at the GBs. Time-resolved photoluminescence measurements showed a strong increase in the carrier lifetime and reduced surface recombination velocity due to the RbF-PDT.[99] In conclusion, it seems that the heavier alkali elements are more effective at reducing the recombination of charge carriers at GBs, interfaces, and surfaces.

When combining a NaF- and a KF-PDT, the increase in cell efficiency is higher compared to a single NaF- or KF-PDT.[100] Hence, a combination of the light alkali element Na with a heavy alkali element (K, Rb, and Cs) is necessary to achieve highest cell efficiencies.

2. Optimization of charge carrier collection in the absorber layer

In a CIGS layer without a Ga grading profile, photo-generated electrons can easily recombine on their way to the

depletion region and to the front contact as the hole concentration is also high. In the case of a Ga grading (more Ga towards the back contact), an internal back surface field is implemented into the CIGS layer which repels electrons from the back contact and drives them towards the space charge region, thereby reducing the recombination of electrons which results in increased short-circuit current density and open-circuit voltage.[39,101] Optimization of this Ga grading is crucial to reach high efficiencies.[89,102] For example, modification of the Ga grading was key to increase the cell efficiency on polyimide substrates from 16% to 18. 7%.[102] On glass substrates, the current density could be increased from 34.8 to 36.6 mA/cm^2.[89] Hence, a precise control of the Ga grading is essential for production of high-efficiency CIGS solar cells. See Fig. 7 for more details.

3. Optimization of the buffer layer

As mentioned above in Sec. III B, the CdS buffer layer has a bandgap of 2.45 eV (Ref. 103) and hence absorbs some part of the UV light which is thus not available for charge carrier generation in the CIGS layer. Hence, reduction of the CdS layer thickness is one way to enhance the quantum efficiency in the UV range of the solar spectrum and thereby increase the photocurrent. An ideal buffer layer for maximum conversion efficiency is therefore one that does not contribute to optical losses. There are two ways to approach this ideal: increase the bandgap of the buffer layer and/or reduce the thickness of the layer (ideally to zero, i.e., eliminate it).

The recently developed alkali fluoride post-deposition treatments described in detail in Sec. III C 1 significantly modify the CIGS surface and therefore the interface between CIGS and the buffer layer. While research and development activities have long been underway to replace or even eliminate CdS as a buffer layer in CIGS solar cells, changing the CIGS surface means that many of these results must be revisited. In fact, one major feature of the efficiency boost enabled by the alkali fluoride PDTs with KF, RbF, and CsF is that the CdS layer thickness can be reduced without losses in V$_{oc}$ or FF. Historically, the first reported development of KF-PDT of the CIGS layer already described this reduction of the CdS thickness as leading to efficiency improvement.[81] Later, it was demonstrated that RbF-PDT enables the CdS layer to be reduced even further.[85] Studies of the initial growth of the CdS layer on the CIGS surface indicate more homogeneous growth and better coverage with an alkali fluoride PDT.[89]

As mentioned above, another option to reduce absorption of UV light in the buffer layer is to replace the CdS layer by another material with a higher bandgap. One candidate is Zn(S,O) with a bandgap of E$_g$ = 3.79 eV.[103] Using this Zn(S,O) layer in combination with a RbF-PDT CIGS layer, an efficiency of 21.0% could be achieved.[89] For Cu(In,Ga)(Se,S)$_2$, an efficiency of 22.0% was realized with a Zn(S,O) layer.[32] In order to improve the band alignment and electron transport across the heterojunction, the Zn(S,O) layer is often coupled with Zn(Mg,O) instead of the non-doped ZnO layer employed with the CdS buffer before deposition of the TCO. The bandgap of Zn(Mg,O) depends on the Mg content and can be increased up to 3.8 eV.[88] This value is higher than the 3.35 eV bandgap of the non-doped ZnO layer and therefore also contributes positively to increased UV transparency. Zn(Mg,O) is also suitable for use with the CdS buffer layer, and the improved quantum efficiency in the UV region has been demonstrated.[104]

Besides Zn(S,O), another promising alternative buffer layer is In$_2$S$_3$. A record efficiency of 18.2% has already been achieved with this material.[105] The bandgap of In$_2$S$_3$ can be tuned from 2.15 eV up to a value of 3.2 eV by adding Na.[106] By using this Na-doped In$_2$S$_3$ buffer layer, a module efficiency of 17.9% was reached on an area of 30 × 30 cm^2.[107]

Finally, an extreme version to get rid of UV light absorption by the buffer layer is to omit the buffer layer completely. For example, Ref. 108 reports on Si-doped CIGS without any buffer layer and a cell efficiency of 15.2%.

D. Process options for manufacturing

Following the stacking sequence of the multilayer structure for CIGS solar cells and modules, as illustrated in Figs. 1 and 9, this section will complement the descriptions before. The focus is on manufacturing-relevant options, like those employed by the currently existing producers as listed in Table IV. Typically, most of the process details are not made public by the producers.

1. Substrate

Most industrial processes use cheap window pane soda-lime glass with a thickness of 1–3 mm for the reasons mentioned in Sec. III B. Specialty glasses are only rarely used in
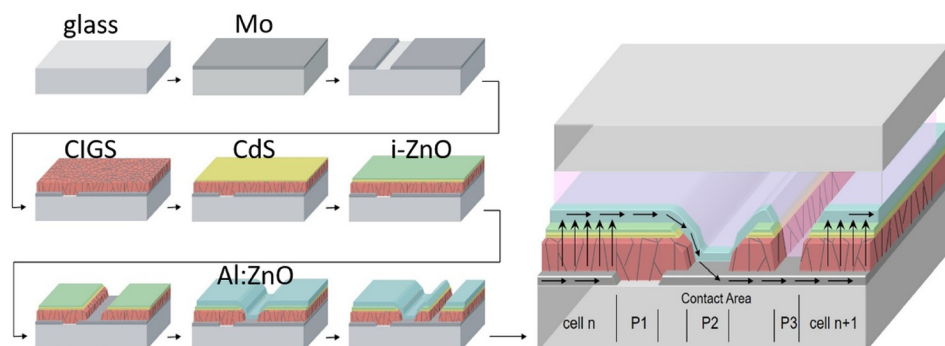
FIG. 9. Illustration of the processing sequence for the production of a thin-film CIGS module: substrate, back contact, isolation cut P1, absorber, buffer layer, open back contact P2, window, isolating cut P3, encapsulation. Due to its widespread use, the monolithic interconnection of individual cells is shown. Further interconnection schemes are discussed in the text.

industrial production so far. Avancis mentions the use of SLG with a higher strain point in Ref. 34.

Industrial approaches for flexible CIGS are pursued by several companies as listed in Table IV. A special approach is successfully implemented by the company Midsummer,[109] working with flexible substrates, but not utilizing large-area processes. Punched stainless steel substrates are covered with a conductive diffusion barrier. The six-inch diameter cells are later used like wafers in silicon PV. They currently report best efficiencies of 16.4% total area.

2. Back contact

As discussed before, molybdenum is the only relevant back contact material for industrial processes at present. There are differences in the preparation routes with respect to sodium permeability or direct sodium supply or with respect to its resistance against $MoSe_2$-formation and the compatibility especially with the absorber process. MiaSolé reports on using a back contact stack of alkali-doped Mo and a thin non-doped Mo layer.[109]

3. CIGS absorber

For the realization of production-relevant in-line processes, coevaporation sources are arranged along the transportation direction and supply Cu, In, Ga, and Se at a constant rate onto the continuously moving substrates.[110] By changing the position and sequence of the elements along the transportation direction, all the previously mentioned CIGS processes can be reproduced. The substrates can either be coated from the bottom or the top, with each option having its own technical challenges. For the evaporation from the bottom, the substrates cannot be fully supported by carriers and thus process temperatures have to remain well below the softening point of the substrate glass. On the other hand, no particles can fall onto the moving substrate.

For optimum homogeneity perpendicular to the transport direction, the evaporation sources can either be arranged as an array of point sources or they can be linear sources.[111]

Just like for the sequential processes, it is hard to find information in the literature about the materials utilization. About 70% utilization is mentioned in a study of simulated evaporation profiles.[111] Concerning the duration of a CIGS production process, it is instructive to know that a cycle time of 2 min was mentioned in Ref. 112 for a CIGS coater for 60 $\times$ 120 cm^2 substrates.

Sputtering of CIGS is used on a large production scale by two companies. While little is known about the process of MiaSolé, the Midsummer process is described in Refs. 109 and 113. The CIGS absorber is composed of multiple layers sputtered from compound targets at temperatures up to 550 °C. The GGI depth profile can be engineered by changing the composition of the targets.

As already mentioned in the section on substrates, there are several elements which are detrimental for the CIGS absorber. Therefore, the purity of the source materials for CIGS deposition has to be subjected to careful quality control. For example, investigations of the influence of Cr contamination on the performance CIGS solar devices in a

production environment showed clear advantages for the use of high purity metals.[114]

As can be seen in Table IV of the existing CIGS producers, different CIGS processes are all used successfully in production. Laboratory cell record values in the last decade have been realized by both coevaporation and sequential processing, indicating that there is not only one viable CIGS deposition technique for production.

4. Buffer layer

As discussed before, CdS is still the buffer allowing the highest efficiencies but which is more and more replaced by alternative materials in industrial production, mainly not only due to legal regulations but also due to its parasitic absorption in the high-energy spectral range.

$Zn(S,O,OH)_x$ buffer layers have been mainly developed by Showa Shell (later Solar Frontier) in Japan,[115] where also legal regulations forbid the usage of Cd in the production of commercial products. In_xS_y, deposited by physical vapour deposition (PVD) is used by Avancis, based in Germany. By the controlled introduction of Na to In_xS_y, the bandgap could be tuned from 2.0 eV up to 2.8 eV, enabling targeted engineering of the band alignment towards the absorber and window layers.[116]

MiaSolé uses PVD of CdS in their production line.[117] Midsummer is employing sputtering of In_2S_3 from a compound target, with additional oxygen incorporation tuned by the amount of oxygen in the Ar/O_2 sputter plasma.[109,113] Evaporation can also be used for In_xS_y, simultaneously with Na for bandgap tuning.

5. Window layer

Doped ZnO layers are the most commonly used window layers,[118] with sputtered Al-doped ZnO (ZAO) and B-doped ZnO (BZO) by MOCVD having the biggest share. Indium tin oxide (ITO) is another option. Further, novel TCOs are investigated by many groups and companies. Among those, especially indium-oxide- and cadmium-oxide-based layers with exceptionally high electron mobilities are most prominent,[119,120] e.g., In_2O_3/ZnO (IZO) or hydrogen-doped In_2O_3 (IOH).[121]

A common way to bypass the tradeoff between improved conductivity and reduced transparency with the increasing TCO thickness is to use grid-assisted current collection. As described in Sec. III E, this allows the use of thinner, more transparent window layers. In order to reap the benefits from the metallic grid carrying the current to the next cell, it is then necessary to control the contact resistance between TCO and the grid, e.g., by the introduction of an additional ITO layer.[113]

E. Module design and production

In Secs. III D 1–III D 5, the different layers of the heterostructure forming the CIGS cells and their production processes were described. This section deals with the options for the interconnection of multiple cells to form modules and includes a tabular overview of current CIGS producers.
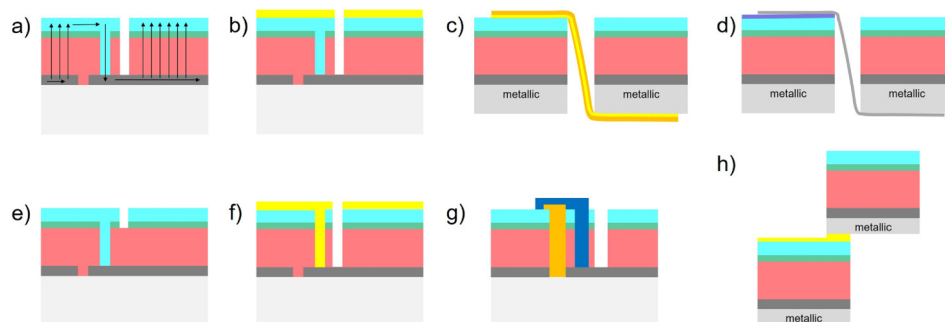
FIG. 10. Different schemes for interconnection, as described in the text: (a) standard monolithic interconnection, (b) grid-assisted current collection, (c) connection by wires embedded in a foil, (d) interconnection like for silicon wafers, (e) P3 by TCO removal, (f) grid-assisted interconnection and current collection, (g) interconnection after all deposition processes, and (h) interconnection by shingling.

Different interconnection schemes are shown in Fig. 10. The most widely used method is monolithic interconnection.[122] The cells are connected by a sequence of patterning steps interlaced with the coating processes (see Fig. 9). A first patterning step known as "P1" interrupts the Mo back contact, separating the back contacts of neighboring cells. A second step "P2" is performed before the window deposition so that at this location, it is deposited on the back contact and thus leads to the electrical connection between the front and back contacts of neighboring cells. The "P3" scribe finalizes the interconnection by separating the front sides of neighboring cells. There are different options for the three scribing processes, either laser processes[123] or mechanical scribing via a stylus. A laser process is usually used for P1, with ablation of the Mo layer either from the top or from behind, through the substrate glass. P2 or P3 by mechanical scribing is a robust process, but it leads to rather wide patterning lines and needs more machine maintenance for having well shaped styluses. As light incident between P1 and P3 does not contribute to the photocurrent, this region is considered the "dead area," and it should be as small as possible.

Laser processes can help to minimize the dead area. A multitude of options exists for the well-controlled P2 laser process of removing CIGS from the Mo by evaporation, and so, it is not possible to give a general recipe. For P3, short-pulse lasers with ps-pulses, or even fs-pulses in the coming years, are used for a lift-off process of the TCO.[124] Different combinations are used for the complete monolithic interconnection, with P1 always being performed by laser, P2 and P3 by mechanical scribing,[125] P2 by laser, and P3 by stylus[126] or all-laser processes.

The dead area typically has a width of 200–250 μm, but smaller widths of, e.g., 100 μm from the middle of P1 to the middle of P3[127] for larger scale modules or even a 70 μm-wide dead area for a module on the lab scale[128] have been reported.

The optimal cell width has to be determined according to complex trade-offs. Narrower cells allow the use of thinner window layers with less absorption losses and thus higher photocurrent, as higher sheet resistances can be tolerated due to the shorter distance the current has to be transported to the next cell, but the larger number of cells for a given module width automatically results in a larger total dead area. On the other hand, a larger number of cells connected in series will result in a higher output voltage. From the system point of view, with many modules being connected in a string with an inverter with limited input voltage, the number of cells should therefore not be too high. Concerning the materials cost of cables, their cross-section and thus the module output current should be minimized—again an advantage to smaller cells.

Another prominent option developed in the last few years is to use grid-assisted current collection,[129] as illustrated in Figs. 10(b) and 10(f), where the current from the cells only has to be transported by the TCO for a shorter distance to the grid fingers, after which it is then transported along the metallic lines to the next cell. Again, the increased dead area caused by shading from the grid lines has to be compensated for by optimizing the window thickness and cell width.

Performing the monolithic interconnection by patterning steps not in the course of the module preparation, but after all the layers have been deposited, is an option which is performed and investigated by several manufacturers.[130,131] A scribe down to the substrate is filled with an insulating material, a conductive paste is coated across this P1-like line and filled into a P2 scribe for connection of the front and back contacts of neighboring cells, and the interconnection is finalized by a P3 scribe [see Fig. 10(g)].

Monolithic interconnection is not mandatory for thin-film modules. When prepared on metallic, potentially even flexible substrates without an electrically insulating barrier, the deposition can be performed on a large area, and then, cells can be cut out, measured, sorted, and then arranged for a connection, e.g., by wires embedded in a foil, as shown in Fig. 10(c). Alternatively, for even larger cells prepared on wafer-sized steel foil substrates, an interconnection like for silicon wafers can be used [see Fig. 10(d)], with grid lines, bus bar, and connecting tapes.[132] Finally, shingling techniques, like that shown in Fig. 10(h), with the (grid supported) front side of one cell directly contacting the backside of the next cell, have been investigated and applied by some manufacturers.

Partial shading of monolithically integrated thin-film modules, which usually are not equipped with bypass diodes for individual cells or groups thereof in a module, can cause some cells to operate in reverse bias and thus cause damaging defects. Scribing lines perpendicular to the patterning lines of the interconnection between the cells lead to electrically isolated sub-modules within the module which are finally connected in parallel. The cells of the sub-modules have a smaller active area, and thus, the area affected by reverse bias damage is reduced for partial shading.[133]

The module assembly is finalized by encapsulation to mechanically protect the thin layer stack and to avoid water damage. A glass-glass-module will typically use an EVA or polyolefin encapsulation foil. A flexible module requires more sophisticated, and typically more expensive, encapsulating foils or multi-layer coatings with very low water vapor transmission rates.

Table IV shows an overview of current producers of CIGS modules, including descriptions of the employed materials and processes, based on information provided through published best module efficiencies and production capacities.

Detailed considerations of production costs for CIGS modules are beyond the scope of this publication. However, some rough information is given in the following.[112,134] Materials make up the largest part of the costs, amounting to 60%. The rest is spread across depreciation (25%), manpower (7.5%), and facility and maintenance (7.5%). Among the materials, the biggest shares are for glass (18%), the junction box (14%), CIGS (13%), targets (13%), and encapsulation foil (8%). Typical numbers that are given for the production of CIGS modules range from 0.40US\$/W_p for current processes and production volumes down to 0.23US\$/W_p for a GW production using improved processes.

CIGS modules are especially interesting in building integrated installations due to their decent black appearance. Figure 11 shows a recent 500 kWp façade installation of CIGS modules in an office building in Basel, Switzerland, realized by NICE Solar Energy.

IV. PEROVSKITE SOLAR CELLS: THE NEWCOMER

Among thin-film PV technologies, metal-halide perovskite (PSC)-based solar cells have only recently emerged. Within a very short time, they have become established as a potentially competitive new route towards next-generation, highly efficient, and cost-effective PV. The technology employs very cheap starting materials, and the processing is favorably low-cost, low-temperature, and compatible with flexible substrates and large-area fabrication. Laboratory-scale cells have surpassed 23% PCE,[1] while module preparation on larger areas is just starting to be developed, see Sec. IV D.[26,144] It still remains to be demonstrated whether or not the perovskite module technology can be successfully developed both technically and economically to the industrial scale. PSC is particularly suited for application as the top cell in stacked tandem devices due to their naturally high optical absorption edge. First, commercial ventures plan to combine semitransparent PSC with conventional silicon cells and modules although any low-gap device including CIGS or low-bandgap perovskite thin-film technologies could also be employed for the bottom cell. Tandem cell configurations increase conversion efficiency since more of the solar spectrum can be exploited, see Sec. IV C and Fig. 15 for more details. The highest reported (but only seldom certified) efficiency values are summarized in Fig. 13 and in Table V. It has to be mentioned that perovskite research is currently an extremely fast-moving research field. Since the first publication of a perovskite solar cell with 3.8% PCE in 2009,[145] more than 5000 scientific articles have been published. More
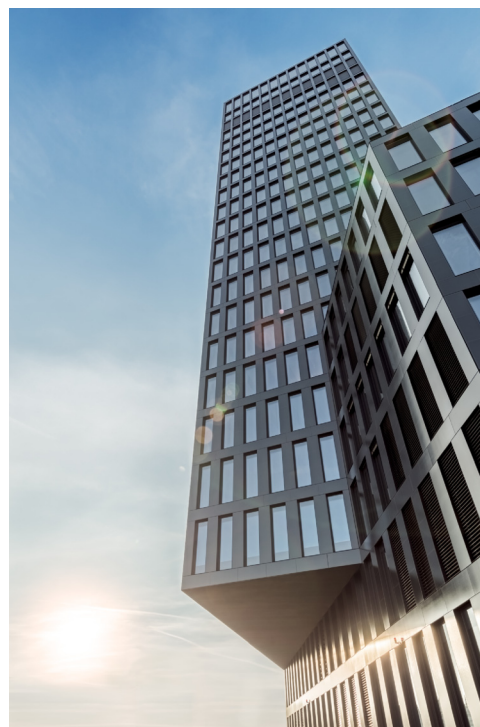

FIG. 11. Example for building integration of CIGS modules, office building in Basel, Switzerland. The picture and information are supplied by Nice Solar Energy, September 2018.

than 2000 publications containing the subject "perovskite solar cell" have been found by the Web of Science (Thomson Reuters) for the year 2016.[146]

As will be described in more detail in Secs. IV A–F, there are several major parameters regarding preparation or materials that tremendously influence the cell efficiency. For example, the crystallinity or overall layer quality already depends on the substrate and bottom contact layer material and roughness, affecting both the hysteresis and efficiency. Furthermore, not only the material composition itself but also the cell geometry and the method of layer preparation can strongly affect the overall efficiency as well (see Sec. IV B).

A. Basics of perovskite materials

Metal-halide perovskite is the name of a material class with the general structure ABX_3, where a hexa-coordinated metal (B) cation occupies the centers of octahedra which share their corner entities (X). Another cation (A) is centered in the void between eight neighboring octahedra. For solar cells, compounds with monovalent halogen anions I^-, Br^-, or Cl^- on the X-site have been most studied. These materials have reasonable bandgaps for highest optical absorption. Accordingly, the A-site should be occupied by monovalent cations and could be anything metallic (e.g., Cs^+, Rb^+) or organic groups such as methylammonium [$(CH_3NH_3)^+$ or abbreviated MA^+] or formamidinium ($[CH(NH_2)_2]^+$, abbreviated FA^+). For charge neutrality, the B-site should be occupied by a divalent cation and should be from the IV_A group of the periodic table, with a strong preference for Pb and alternatively Sn, see Fig. 12 for details.

TABLE V. Perovskite record solar cells (single cells, no tandems) with most relevant architecture (n-i-p or p-i-n on mesoporous TiO$_2$ or on planar transport layers) and process details. The absorber column only describes the principle cations and anions without regard to stoichiometry. Mostly certified efficiencies (marked with "*") or values measured under stabilized maximum power point conditions (marked with "#") are listed. With only a few exceptions, the highest efficiencies are achieved with the classical n-i-p geometry on TiO$_2$. Most cell areas are still in the 0.1 cm^2 range. BCP: Bathocuproine, BPhen: Bathophenanthroline, CB: chlorobenzene, DE: Diethylether, DMF: dimethylformamide, F4-TCNQ: 2,3,5,6-Tetrafluoro-7,7,8,8-tetracyanoquinodimethane, F6-TCNNQ: 2,2′-(perfluoronaphthalene-,6-diylidene)di-malononitrile, FA: Formamidinium, FTO: Fluorine-doped indium tin oxide, Gua: guanidine, IDIC: 2,2′-((2Z,2′Z)-((4,4,9,9-tetrahexyl-4,9-dihydro-s-indaceno[1,2-b:5,6-b′]dithiophene-2,7-diyl)bis(methanylylide-ne))bis(3-oxo-2,3-dihydro-1H-indene-2,1-diylidene))dimalononitrile, ITO: indium tin oxide, MA: methylammonium, meso: mesoporous, PCBM: [6,6]-Phenyl-C61Buttersäuremethylester, PhIm: 1,N4-bis(tri-p-tolyl-phosphoranylidene)benzene-1,4-diamine, PMMA: polymethylmethacrylate, PS: polystyrene, PTAA: polytriarylamine, Poly-tpd: Poly(N,N′-bis-4-butylphenyl-N,N′-bisphenyl)benzidine, rGO: reduced graphe-neoxide, spiro-OMeTAD: 2,2′,7,7′-Tetrakis-(N,N-di-4-methoxyphenylamino)-9,9′-spirobifluorene, TaTm: N4,N4,N4′′,N4′′-tetra([1,1′-biphenyl]-4-yl)-[1,1′:4′,1′′-ter-phenyl]-4,4′′-diamine, SAM: self-assembling monolayer, TL: toluene, and Tu: Thiourea, Z26: 4,4′-((1E,1′E)-(3,4-dimethoxythiophene-2,5-diyl)bis(ethene-2,1-diyl))bis(N,N-bis(4-methoxyphenyl))aniline.

Configuration	TCO	Interlayer 1	Absorber	Deposition method	Interlayer 2	Back contact	PCE (%)	Cell size (cm^2)	Year	References
Standard n-i-p meso-porous TiO$_2$	FTO	meso-TiO$_2$	FAMAPbIBr	spin, 2-step	PTAA	Au	20.1*	0.16	2015	280
	FTO	meso-TiO$_2$	FAMAPb IBr	spin, CB drip	spiro-OMeTAD	Au	19.7*	0.16	2016	170
	FTO	meso-TiO$_2$	CsFAMAPbIBr	spin, CB drip	spiro-OMeTAD	Au	21.1#	0.16	2016	167
	FTO	meso-TiO$_2$	MAPbI$_3$	spin, DE drip	spiro-OMeTAD	Ag	20.4	0.13	2016	281
	FTO	meso-TiO$_2$	FAMAPbIBr	spin, drip with PMMA in CB/TL	spiro-OMeTAD	Au	21.0*	0.11	2016	187
	FTO	meso-TiO$_2$	RbCsFAMAPbIBr	spin, CB drip	spiro-OMeTAD/(PTAA)	Au	21.6#	0.16	2016	166
	FTO	meso-TiO$_2$	RbCsFAMAPbIBr	spin, CB drip	spiro-OMeTAD/(PTAA)	Au	19.0#	0.50	2016	166
	FTO	meso-TiO$_2$	FAMAPbIBr	spin, 2-step + TL drip	PTAA	Au	20.1#	0.10	2016	282
	FTO	meso-TiO$_2$	FAMAPbIBr	spin, 2-step +CB drip	spiro-OMeTAD	Au	21.3	0.16	2017	188
	FTO	meso-TiO$_2$	MAPbI$_3$	spin, TL drip	PTAA	Au	19.7#	0.10	2017	160
	FTO	meso-TiO$_2$	FAMAPbIBr	spin, 2-step	PTAA	Au	22.1*	0.09	2017	185
	FTO	meso-TiO$_2$	CsFAMAPbIBr	spin, CB drip	spiro-OMeTAD	Au	20.8	0.25	2017	191
	FTO	meso-TiO$_2$	CsFAMAPbIBr	spin, CB drip	spiro-OMeTAD	Au	18.0	1.00	2017	191
	FTO	meso-TiO$_2$	FAMAPbIBr	spin, CB drip	spiro-OMeTAD	Au	20.6	0.16	2017	283
	FTO	meso-TiO$_2$	FAMAPbIBr	spin, CB drip	Z26	Au	20.1	0.16	2017	283
	FTO	meso-TiO$_2$	CsFAMAPbIBr	spin, CB drip	spiro-OMeTAD	Au	20.5#	0.16	2017	190
	FTO	meso-TiO$_2$	CsFAMAPbIBr	spin, CB drip	CuSCN/rGO	Au	20.2#	0.16	2017	190
	FTO	meso-TiO$_2$	KCsFAMAPbIBr	spin, CB drip	spiro-OMeTAD	Au	21.3#	0.11	2018	284
Standard n-i-p pla-nar transport layer	FTO	SnO$_2$	CsFAMAPbIBr	spin, CB drip	spiro-OMeTAD	Au	20.8#	0.16	2016	285
	ITO	C$_{60}$:PhIm/C$_{60}$	MAPbI$_3$	coevaporation	TaTm/TaTm:F6-TCNNQ	Ag	20.3	0.10	2016	286
	ITO	TiO$_2$-Cl	CsFAMAPbIBr	spin, CB drip	spiro-OMeTAD	Au	19.5*	1.10	2017	287
	ITO	TiO$_2$-Cl	CsFAMAPbIBr	spin, CB drip	spiro-OMeTAD	Au	20.1*	0.05	2017	287
	FTO	TiO$_2$/La:BaSnO$_3$	MAPbI$_3$	spin, TL drip	PTAA	Au	21.2#	0.10	2017	160
	FTO	TiO$_2$	CsMAPbICl	coevaporation	spiro-OMeTAD	Au	19.9#	0.09	2017	288
	ITO	SnO$_2$	FAMAPbIBr	spin, 2-step	spiro-OMeTAD	Au	20.1	1.00	2017	186
	ITO	SnO$_2$	FAMAPbIBr	spin, 2-step	spiro-OMeTAD	Au	21.6	0.07	2017	186
	ITO	C$_{60}$-SAM-SnO$_x$-PCBM	FAMAPbIBr	spin, CB drip	Polymer PDCBT/Ta-WOx	Au	21.1#	0.10	2017	189
	ITO	EDTA-SnO$_2$	FACsPbI$_3$	spin, CB drip	spiro-OMeTAD	Au	21.5*	0.11	2018	289
Inverted p-i-n pla-nar transport layer	ITO	PTAA	MAPbI$_3$	spin, 2-step	PCBM/C$_{60}$/BCP	Al	19.4	0.08	2016	290
	ITO	PTAA:F4-TCNQ	MAPbI$_3$	spin, DMF anneal	PS/C$_{60}$/BCP	Al	20.3#	0.1	2016	291
	ITO	PTAA	MAPbI$_3$	spin, 2-step	IDIC/C$_{60}$/BCP	Cu	19.4	0.1	2016	292

TABLE V. (Continued.)

| Configuration	TCO	Interlayer 1	Absorber	Deposition method	Interlayer 2	Back contact	PCE (%)	Cell size (cm^2)	Year	References
	ITO	PEDOT:PSS	MAPbI$_3$	spin, 2-step	PCBM70	Ca/Al	19.6#	0.10	2017	201
	ITO	Cu(TuI)I	MAPbI$_{3-x}$Cl$_x$	spin, CB drip	C$_{60}$/BCP	Ag	19.9#	0.1	2017	293
	ITO	PTAA	CsFAMAPbIBr	spin, DE drip	PS/C$_{60}$/BCP	Cu	20.4#	0.06	2017	202
	ITO	PTAA	FAMAPbIBr	spin, TL drip	choline chloride/C$_{60}$/BCP	Cu	20.6*	0.07	2017	203
	ITO	PTAA	FAMAPbIBr/GuaBr	spin, CB drip	PCBM/C$_{60}$/BCP	Cu	20.9*	0.05	2018	294
	ITO	PTAA:F4-TCNQ/PS	MAPbI$_3$	Spin, 2-Butanol drip	PCBM/BPhen	Al	20.1#	0.12	2018	295
	ITO	Poly-tpd:F4-TCNQ/PMMA	MAPbI$_3$	Spin, 2-Butanol drip	PCBM/BPhen	Al	20.0#	0.12	2018	295
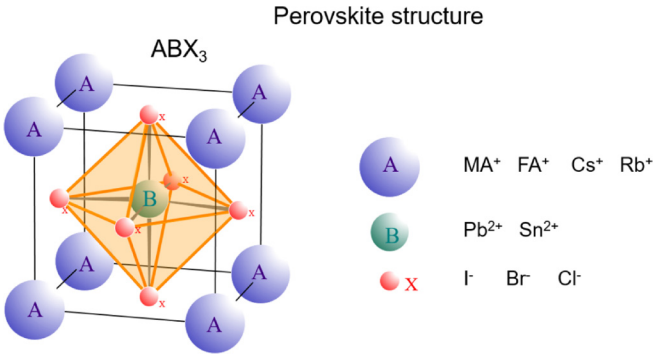
FIG. 12. Octahedral ABX$_3$ structure of metal halide perovskite.

There is only a certain range of ionic radii that allows a stable three-dimensional ABX$_3$ perovskite crystal structure. The relationship $t = \frac{R_A + R_X}{\{\sqrt{2}(R_B + R_X)\}} \approx 1$ must be fulfilled for the ionic radii R$_A$, R$_B$, and R$_X$ of the A, B and X ions,[147] where t is the tolerance factor first introduced by Goldschmidt.[148] For a stable, six-fold coordination of the octahedral structure BX$_6$, the ratio of the radii of the B- and X-site ions must be within the range of $0.442 < R_B/R_X < 0.895$. Smaller values of t induce lower symmetry, while too large t values cause formation of a 2D layered structure instead of 3D geometries.

The most commonly used material for photovoltaic applications is methyl-ammonium lead triiodide CH$_3$NH$_3$PbI$_3$ or MAPbI$_3$. It undergoes two phase transitions, the first from orthorhombic to tetragonal at temperatures above 160 K and the second to cubic above 327 K. Interestingly, the performance of the solar cell is not severely affected by the phase transitions.[149] However, the general instability of the crystal lattice might be a critical issue on a longer time scale.

The bandgap of MAPbI$_3$ is reported to be around 1.55–1.6 eV, corresponding to an absorption onset at $\lambda = 780$ nm. Its absorption coefficient was estimated to be 1.5×10^4 cm^{-1} at 550 nm (Ref. 150) and allows full absorption of solar photons with energies higher than the bandgap within only 1 μm of material.

An important feature of perovskite material is the low excitonic binding energy of approximately 30 meV as already measured in 1994 by Hirasawa *et al.*,[151] allowing an instantaneous separation of bound excitons into free electron-hole pairs by thermal activation at room temperature. In addition, the diffusion lengths[152,153] and accordingly the carrier lifetimes are exceptionally high (μs range[154]). Together with sufficiently high electron and hole mobilities in the range of 10–40 cm^2/V s,[155] simple and fast carrier extraction at the electrical contact layers is practically guaranteed.

1. Bandgap tunability

Metal-halide perovskite solar cells quickly attracted attention during the last few years not only because of their high efficiencies but also due to the naturally already relatively high bandgap of MAPbI$_3$ and their easy tunability by ion replacement, making highly efficient semitransparent and tandem structures feasible, see Fig. 13(a). The bandgap of the ABX$_3$ perovskite is most strongly influenced by exchanging the species on the X-site, i.e., by adjusting the
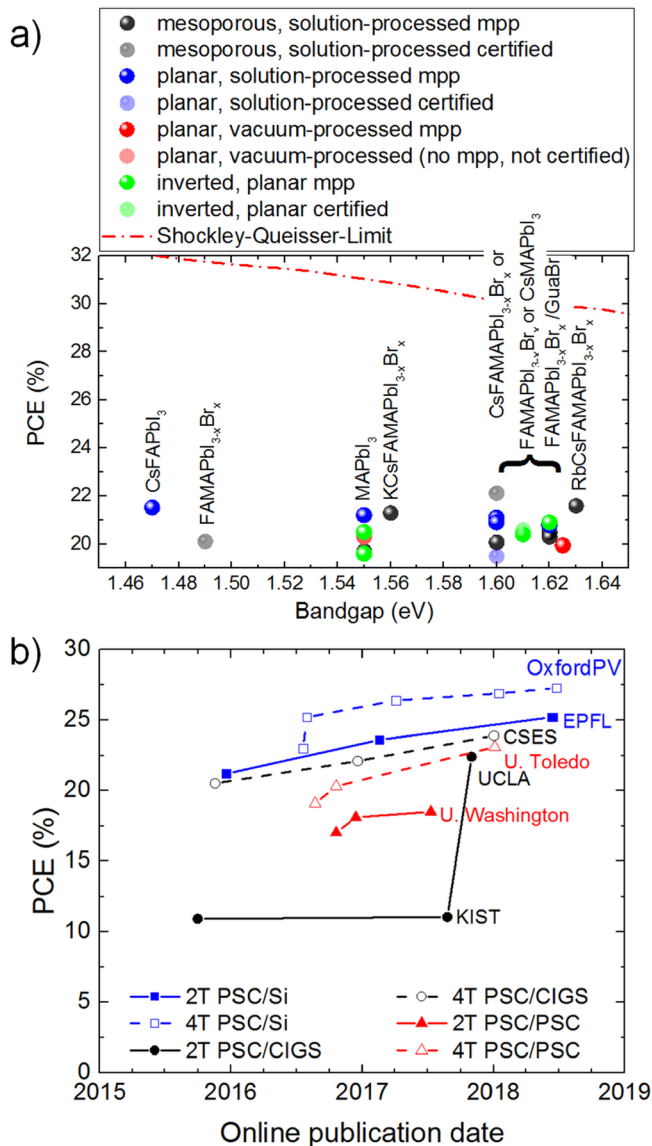
FIG. 13. (a) Reported efficiencies for record perovskite cells with different chemistries and their corresponding bandgap as labelled and different geometries as indicated by the symbol color. The values are included for pure iodide PSC with MA, CsMA, or FA or advanced multi-cation mixtures like RbCsMAFA-Pb-IBr with iodide/bromide halide mixtures. The theoretically achievable efficiency according to the Shockley-Queisser limit is indicated by the dashed line. (b) Record efficiencies for tandem structures of perovskite top cells in combination with Si, CIGS, or perovskite bottom cells.

halogen anion. Replacing the largest anion I^- by the smaller Br^- or Cl^- anion proportionally shifts the bandgap to higher energies, from 1.55 eV for $CH_3NH_3PbI_3$ to 2.3 eV for $CH_3NH_3PbBr_3$ or up to 3.1 eV for $CH_3NH_3PbCl_3$.[156,157]

To a smaller extent, the bandgap is also tunable by modifying the species on the A-site due to lattice dilation when organic groups replace metallic cations. The ionic size of the A-site cation increases from 1.80 Å for Cs^+ to 2.17 Å for $(CH_3NH_3)^+$ and to 2.53 Å for $[CH(NH_2)_2]^+$, so that the unit cell size of $APbI_3$ increases from 222 Å to 248 Å and to 256 Å, respectively. Accordingly, the bandgap reduces from 1.73 eV for $CsPbI_3$ to 1.55 eV for $CH_3NH_3PbI_3$ and to 1.48 eV for $CH(NH_2)_2PbI_3$.[158]

Similarly, the B-site cation also influences the bandgap. With Sn^{2+} replacing the Pb^{2+} cation, which is especially attractive for developing lead-free devices, the bandgap is

lowered down to 1.24 eV for $CH_3NH_3SnI_3$.[159] However, as shortly discussed in Sec. IV E, tin is a very unstable and difficult material to work with. Figure 13(a) lists recent record efficiencies reported for different material compositions and resulting bandgaps. In fact, the highest efficiencies have bandgaps around 1.6 eV and exhibit a smaller efficiency gap compared to the theoretically possible efficiency as calculated by the Shockley-Queisser limit.[7]

2. Multi-cation approaches

Multi-cation approaches have been increasingly investigated for reasons besides modification of the bandgap. Classical $MAPbI_3$ cells have surpassed the 20% threshold, with an exceptional 21.2% reported by Shin *et al.*,[160] but suffer from instability which is to some extent also related to phase instability and phase transitions near room temperature.[161] Photo-induced trap formation[162] and halide segregation have also been reported for the case of mixed halide perovskite in the $MAPbB_xI_{(3-x)}$ system.[163] Hence, higher efficiencies and improvements in stability were expected and proven in mixed cation approaches by adding more inorganic elements and increasing the entropy of mixing, which should stabilize ordinarily unstable materials.[164–167] Unfortunately, pure Cs-based $CsPbI_3$ crystallizes only in a photo-inactive δ-phase at room temperature.[168]

After the early work combining FA and MA in the form of mixed $MAPbBr_3$ and (FA lead iodide) $FAPbI_3$ by Jeon *et al.*, who achieved up to 19.0% for standard n-i-p architectures (i.e., film deposition starts with the negative contact electrode and is completed by the positive contact electrode, see Fig. 15) measured in the reverse direction,[169] efficiencies could be increased to 20.8% by Bi *et al.* by a mixture of FAI, PbI_2, MABr, and $PbBr_2$ for standard n-i-p geometry on mesoporous TiO_2.[170] Their work demonstrated that a small amount of MA is already sufficient to induce a preferable crystallization into the photoactive "black" phase of FA perovskite, resulting in a more thermally and structurally stable composition than the pure MA or FA compounds.

By including the even smaller inorganic Cs ion, Saliba introduced the triple cation Cs/MA/FA configuration with the overall composition $Cs_5(MA_{0.17}FA_{0.83})_{95}Pb(I_{0.83}Br_{0.17})_3$ in 2016. Adding small amounts of Cs resulted in larger grains of high-purity perovskite with higher long-term stability and higher reproducibility, resulting in a stabilized record efficiency of 21.1%.[167] Shortly afterwards this approach was extended to also include Rb,[166] which is already outside the theoretical Goldschmidt tolerance limit due to its ionic radius, but improved stabilized efficiency up to 21.6%.

Various additives have been suggested to improve stability, hysteretic behavior (see Sec. IV B) and efficiency, such as potassium[171] or, e.g., direct inclusion of fullerenes into the perovskite layer[172] as summarized in Ref. 173.

B. Film deposition and cell architectures of perovskite devices

1. Film deposition

PSC film deposition techniques can roughly be classified in vacuum-based physical vapor deposition, solution-based

vacuum-free techniques, such as ultrasonic spray coating, spin coating, doctor blading, printing, dipping, and slot die coating, and combinations of both. Solution-based techniques are far more often investigated in the literature and should allow lower production costs. Due to their susceptibility to moisture, high-quality reproducible perovskite films are normally handled in inert gas (nitrogen) in glovebox systems.

The film formation and morphology of the perovskite layer are of highest importance for reproducibility, hysteresis strength, solar cell performance, and stability. Generally speaking, dense layers of large perovskite crystals without secondary phases are desired. Controlling the crystal growth from solution is managed by various methods, based either on a one-step deposition (growth-dominated) or on a two-step deposition (nucleation-dominated), see Fig. 14 for details. In the first case, all constituents are dissolved in one single solution. In the second case, two separate solutions of PbI$_2$ and MAI are prepared and deposited sequentially so that the perovskite formation takes place only after the deposition.[174] The one-step method most often takes place via an induced supersaturation of the wet precursor film to trigger a self-seeded crystallization as proposed by the LaMer theory.[175] To initiate the nucleation, the concentration in solution has to be increased in a well-controlled way by typically initiating a very fast drying in a nitrogen flow,[176] by dripping

a second solvent ("antisolvent") onto the wet precursor film,[177,178] or by immersing the complete sample in an suitable second solvent, called solvent-solvent extraction.[179] In the case of antisolvent dripping, the second solvent does not dissolve the perovskite but is miscible with the original solvent. Its task is to rapidly reduce the solubility of the perovskite in the mixed solvent, initiate the formation of an intermediate complex, and thereby promote fast nucleation.[177] While the first two methods usually finish with a thermal annealing step in the range of 80–120 °C to improve crystallinity and to remove residual organic compounds, the solvent-solvent extraction method enables a very fast room-temperature crystallization. The perovskite precursor is dissolved in a high boiling point (204 °C) first solvent (N-methyl-2-pyrrolidone NMP), while the wet film is immersed into a bath of low boiling point (35 °C) second solvent (diethyl ether) which removes the excess NMP in the film.[179]

The crystal growth can be additionally promoted by solvent annealing in a solvent atmosphere[180] or by annealing in controlled humidity.[181] A detailed review can be found in Ref. 182.

2. Perovskite solar cell architectures

Perovskite solar cells can be prepared in various cell architecture subtypes as well as by various deposition methods. Common to nearly all of them is that the cells are prepared in the superstrate configuration, i.e., that the sunlight reaches the absorber layer through the transparent mechanical support (e.g., glass) and conductive contact layer. Rare examples of the substrate configuration are the report by Troughton *et al.* on titanium foil[183] and semitransparent cells[184] that can naturally be illuminated from either side, compare Fig. 15.

A perovskite cell stack typically comprises a thin absorber layer of ~300–400 nm thickness sandwiched between adjacent hole- or electron-selective layers (HTL or ETL, respectively) and the contact layers. The main distinctions in architecture are the polarity of the contacts and sequence of the HTL and ETL absorber layer, leading to either an n-i-p (or "standard") or a p-i-n (or "inverted") structure. In addition, both configurations can be modified to create semitransparent cells by substituting the corresponding opaque metal contact layers with transparent alternatives (see Sec. IV C).

As perovskite cells are historically derived from dye sensitized solar cells, **n-i-p** is the most often used configuration with still the highest reported record efficiencies exceeding 20%,[166,185–191] as is also evident from the record efficiencies listed in Table V. Typically, fluorine-doped tin-oxide (FTO)-coated glass is covered by an ETL either consisting of a simple dense layer of titanium oxide or by an additional mesoporous TiO$_2$ layer which enhances the interface area. The additional mesoporous layer can reduce hysteresis, but requires high-temperature curing steps (see Ref. 192 for a review). After perovskite deposition, an HTL made from Spiro-OMeTAD [2,2′,7,7′-Tetrakis-(N,N-di-4-methoxyphenylamino)–9,9′-spirobifluorene] is coated,[193] followed by a gold or silver back contact. Efforts
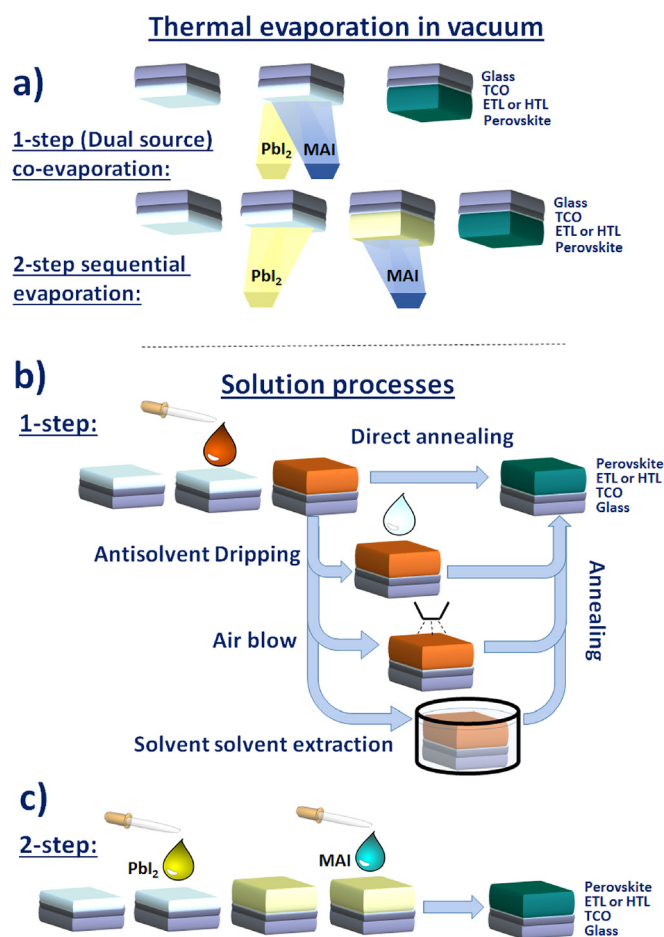

FIG. 14. Main preparation routes for perovskite solar cells: (a) vacuum evaporation, (b) 1-step solution processes, and (c) 2-step solution processes.
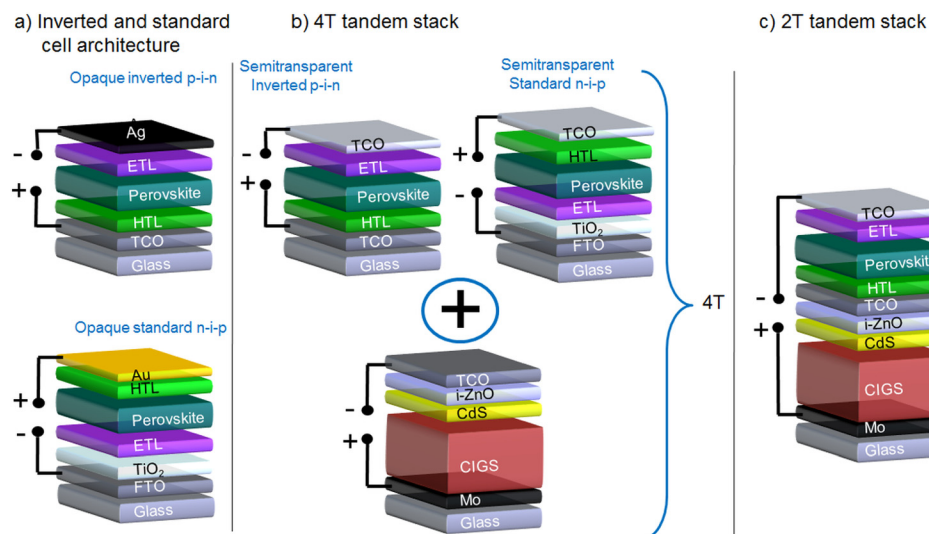
FIG. 15. (a) Inverted and standard single cell architecture, (b) 4-terminal (4T) tandem cell stack with the CIGS bottom cell and semitransparent perovskite top cells, and (c) 2-terminal (2T) tandem cell stack with the inverted perovskite top cell and the CIGS bottom cell.

are presently underway to replace the costly Spiro-OMeTAD by cheaper materials with ideally also higher transmittance and stability; for a review, see, e.g., Ref. 194.

In parallel, expertise generated by the research of organic solar cells has led to the development of **p-i-n** planar devices,[195] typically starting with indium tin oxide (ITO)-coated glass covered by the HTL poly(3,4-ethylenedioxythiophene) polystyrene sulfonate (PEDOT:PSS)[196] or, e.g., PTAA[194,197] or NiO$_x$.[198,199] The subsequent perovskite absorber layer is covered by an ETL typically made from fullerene-based materials such as [6,6]-phenyl-C61-butyric acid methyl ester (PCBM)[200] or, e.g., ZnO nanoparticles.[199]

This configuration has reached record efficiencies exceeding 20%,[201–203] slightly below those of n-i-p structures, but often shows less hysteretic behavior. As it does not need any high-temperature curing of TiO$_2$, this process is potentially very simple and cost-effective.

Additional particular solar cell architectures comprise the transition to semitransparent cell stacks (see Sec. IV C) and complete tandem stacks.

"Hysteresis" describes the undesired effect observed for most perovskite solar cells that the shape of current-voltage (IV) measurements depends on the scan direction and the scan rate, making it difficult to determine relevant cell parameters unambiguously. Hence, to obtain comparable and industrially relevant results, it is necessary to develop measurement standards and aging tests as discussed by Saliba.[204] In early publications, the apparently highest efficiency values were often reported, determined when measured quickly in the "down" direction from positive to negative bias voltage values. Nowadays, it is also recommended to provide the stabilized value as measured at the maximum power point (mpp) for several minutes. In fact, all record perovskite devices are (nearly) hysteresis-free, but even the certified efficiency records are classified as "not stabilized". In Table V, only certified values or values that have been measured stabilized at mpp are listed.

The physical cause of the hysteresis behavior is still not completely understood, and several possibilities have been proposed: ion migration,[205–209] ferroelectricity,[210] a photo-induced capacitive effect,[211] charge trapping,[212] and

combinations thereof.[213] It was observed that contact materials as well as interlayers have a strong influence on the occurrence of hysteresis.[206,212,214] Additionally, it was found that pre-biasing conditions have an immense impact on the IV measurements due to charge accumulation at the electrode(s).[205,215] As mentioned above, hysteresis depends strongly on the cell architecture. Planar n-i-p perovskite devices (standard architecture) are more prone to hysteresis than mesoporous n-i-p or inverted planar p-i-n perovskite solar cells.[216]

C. Semitransparent perovskite cells and tandem approaches

Semitransparent perovskite solar cells can be roughly classified into three categories: (a) neutral-colored (e.g., for BIPV), (b) bifacial cells, and (c) top cells for tandem applications.

Neutral-colored (or translucent) cells are implemented by only partly covering the substrate with perovskite absorber layers already by means of the deposition process, e.g., by island (dewetting)[217,218] or colloidal self-assembly combined with plasma etching[219] deposition processes, or by removal of the material after deposition, e.g., by partial area ablation (by laser or mechanical). Obviously, the PCEs are strongly related to the coverage and transmittance, and the reported values are therefore in a lower range. Efficiencies between 3.5% and 10.3% were reported for the partial deposition processes. Efficient modules (4 cm^2 area) with a PCE of 5.4%–13.1% and an average transmittance (AVT) of 37%–7% were demonstrated by partial removal processes.[220] Free-standing semitransparent or translucent cells are also deployed in bifacial architectures enabling the absorption from both sides of the cell.[221–223] Hence, a reflective surrounding increases the current (e.g., by 13.5% with a white paper placed behind[224]) and therefore also the overall power generation.

Efficient semitransparent cells containing various transparent electrodes with (non-certified) PCEs in the range of 14.5% up to 18.1%[225] were reported in the literature recently. It is important to note that the differences in the

PCE are at least partly due to different cell sizes and bandgaps of the absorber layers.

Transparent electrodes can be realized by using thin metal layers[226] or solution-processed silver nanowires,[227] but in most cases, transparent conducting oxides (TCOs, especially ITO) are employed on both sides of the solar cell. ITO at both sides was reported in Refs. [228] and [229]. Other options are SnO_2/ZTO (certified on 1 cm^2 area),[230] ITO and IZO,[225,231] ITO/IO:H and IZO[232] or ITO,[233] ITO and ZAO,[234] ITO and FTO,[235,236] or an ITO-free device with ZAO and In_2O_3:H.[184] Different contact materials can improve the IR transmittance (e.g., IZO compared to FTO), but also implement advanced optical light management schemes minimizing overall reflection and maximizing sub-bandgap transmission.[237] Bandgap grading was also suggested to improve the overall efficiency and long-term stability.[234]

The current record for semitransparent cells was achieved by Shen *et al.* with 18.1% for a standard bandgap configuration of 1.62 eV with the composition $Cs_{0.05}Rb_{0.05}FA_{0.765}MA_{0.135}PbI_{2.55}Br_{0.45}$ and 16.0% for an increased bandgap of 1.75 eV with the composition $Cs_{0.17}Rb_{0.05}FA_{0.75}MA_{0.15}PbI_{1.8}Br_{1.2}$.[225] The devices employed the n-i-p configuration with mesoporous TiO_2 on ITO, followed by the absorber and Spiro-OMeTAD, MoO_x, IZO, gold grid fingers, and an antireflective coating of MgF_2. The transmittance of the perovskite cell was approximately 80% above a wavelength of 800 nm in both cases.

1. Tandem approaches

Semitransparent wide-bandgap perovskite cells are especially interesting in **tandem combination** with a second low-bandgap solar cell for a more efficient use of the solar spectrum. Such combinations are naturally attractive with the most-established low-bandgap solar cells such as silicon or CIGS, or even low-bandgap perovskites. In contrast to bifacial cells, the semitransparent cells for tandem applications should not only have very high efficiencies but also need to be highly transparent below their optical bandgap in order to enable a maximum possible transmission of photons to the small-bandgap bottom cell in the tandem stack for further power conversion. Two basic architectures are used: the two-terminal (2T) and the four-terminal (4T) architecture, compare Figs. 15(b) and 15(c). In the 2 T tandem cell, the top cell is directly deposited on the transparent electrode of the bottom cell, whereas in the 4 T tandem cell, the top and bottom cells are prepared individually and are then stacked mechanically. In contrast to the 2 T architecture where the top and bottom cells are connected in series, the 4 T architecture does not require current matching since the currents of the top and bottom cells are accessed separately. On the other hand, in the 2 T tandem cell, the top and the bottom cells "share" the semitransparent electrode in the middle (recombination layer) and only one glass substrate is needed. The most commonly used materials for this recombination layer or the transparent electrode are sputtered TCOs like IZO, IO:H, ITO, or ZAO, but there are also other promising materials like solution-processed silver nanowires,[227] thin evaporated metal layers,[226] or hydrogenated nano-crystalline

silicon,[231] which are deposited by plasma-enhanced chemical vapor deposition. So far, the best efficiencies were made with the combination of a silicon bottom cell and a perovskite cell on top in the 2 T (23.6%,[230] certified by NREL) as well as in the 4 T architecture (26.7%[227]). The recent development of tandem efficiencies is visualized in Fig. 13(b). Concerning the perovskite absorber layer, there are many different perovskite compositions from simple $MAPbI_3$ to combinations of different anions and cations like Cs, Rb, FA, I, Br, and Sn to manipulate the bandgap, as discussed in Sec. IV A and shown in Fig. 13(a).

2. Si + perovskite tandems

So far, most tandem cell approaches were made by combining silicon with perovskite in both architectures. In the 2 T tandem structure, efficiencies over 22% were reached,[230,231,238] with a record efficiency of 25.2%[239] on 1.4 cm^2 as certified by Fraunhofer ISE. In the 4 T architecture, higher efficiencies were reached, with PCEs > 25%[227,229,233,237] and a record efficiency of 27.3% PCE has been achieved by Oxford PV.[240]

3. CIGS + perovskite tandems

The direct deposition of perovskite layers on CIGS is challenging due to film formation on the non-flat CIGS surface and possible interaction with adjacent layers or impact on crystallization. However, in 2015, Todorov *et al.* presented a first remarkable study on a completely solution-processed monolithic 2 T CIGS-perovskite cell. Cu(In,Ga)Se$_2$ was made from a hydrazine-based solution with an optimized lower bandgap of 1.04 eV, while the perovskite bandgap was adjusted via the I/Br ratio during a 2-step methylammonium halide treatment. As ZnO is known to react with the perovskite at elevated temperatures, degrading both the contact layer and the absorber layer, ITO was used as an intermediate contact. They could already achieve a tandem efficiency of 10.9%.[241]

A slightly better efficiency of 11.0% was reported recently for electrodeposited $CuInSe_2$.[242] In that case, $MAPbI_3$ was directly deposited on the intermediate contact made from i-ZnO/ZnO:Al + PEDOT. The top contact was PCBM/ZnO-np and ZnO:Al. Very recently, the efficiency of 2T-CIGS-perovskite tandems could be drastically improved from 11% to 22.4% by UCLA.[26]

More success in terms of overall efficiencies has already been reported for 4 T tandem approaches. Efficiencies of over 22% were achieved in the 4 T architecture[184,225,234] with a record efficiency of 23.9% [stabilized MPP on 0.3 cm^2 (Ref. [225])] in combination with CIGS. Fu *et al.* demonstrated an inverted semitransparent cell with 16.8% and a graded Br content for bandgap grading and applied a real stacked configuration, i.e., sample sizes were identical for the CIGS and perovskite cells.[234] With that, they achieved a 22.7% 4 T efficiency.

4. Perovskite + Perovskite tandems

When combining two perovskite layers with different bandgaps, the absorber layer with a smaller bandgap of

1.2–1.3 eV was made by partly replacing lead by tin and individual efficiencies up to 17.2% [stabilized MPP on 0.1 cm^2 (Ref. 236)] were reached. The best efficiency in the 2 T architecture was 18.5% [stabilized MPP on 0.14 cm^2 (Ref. 243)] and was achieved by combining cells with 1.82 eV [$MA_{0.9}Cs_{0.1}Pb(I_{0.6}Br_{0.4})_3$] and 1.22 eV ($MAPb_{0.5}Sn_{0.5}I_3$) using the inverted stack with ITO/PEDOT:PSS as the recombination layer.

Similar to the aforementioned combinations with CIGS or silicon, better efficiencies were reached with 4 T tandems with up to 23.1% [stabilized MPP: 22.9% on 0.1 cm^2 (Ref. 236)] by combining individual efficiencies of 15.5% [1.75 eV, $FA_{0.8}Cs_{0.2}Pb(I_{0.7}Br_{0.3})_3$] and 17.2% [1.25 eV, $(FASnI_3)_{0.6}(MAPbI_3)_{0.4}$] and employing paraffin oil as a coupler between top and bottom cells.

D. Flexible and large-scale approaches for perovskite devices

An additional advantage of the moderate process temperatures used in perovskite cell technology is the possibility to also use **flexible transparent substrates** based on PET or PEN foils, enabling low-cost roll-to-roll fabrication and new innovative flexible applications.

Efficiencies on PET/ITO substrates have reached 18.1%;[244] 14% on PEN/ITO with flexible encapsulation.[245] Repeated bending stability can be better achieved with ITO-free alternatives with 12.3% on PET/PEDOT:PSS[246] or for graphene contacts[247,248] with efficiencies up to 16.8% for PET/graphene, allowing 5000 bending cycles with bending radii of 4 and 2 mm.[247] In addition, using very thin 20 μm-thick PET substrates allows very high power output per weight of about 5 W/g.[248] Flexible perovskite devices are being developed for commercialization, e.g., by Saule Technologies.

1. Large-scale approaches and modules

The vast majority of perovskite publications still report only on small lab-scale solar cells, most often even with cell areas far below the 1 cm^2 area. In 2015, Chen *et al.* certified the first 1 cm^2 PSC with 15.0% PCE, which was listed in the credited Solar Cell Efficiency Tables (Version 46).[249,250] Currently, the efficiency record of 1 cm^2 PSC has been raised to 20.9%,[26] while the small-area record is 23.3% in the NREL efficiency chart.[1] However, upscaling from a 1 cm^2 device to mini-modules >10 cm^2, the certified efficiency record is limited to 17.25%.[26] As time progresses, the number of published works on large-scale devices, especially on modules, is steadily increasing. A first challenge is that the typical deposition method for high-efficiency cells (dripping or antisolvent process—see Sec. IV B and Fig. 14) is not easily transferred to large-area coatings. For details, see, e.g., reviews in Refs. 251 and 252. The reported efficiencies are still mainly in a range of 10%–12% for modules.

To mention some recent exceptions exceeding 15% efficiency: Yang *et al.* reported on a four-cell $MA_{0.7}FA_{0.3}PbI_3$ perovskite module with a stabilized power conversion efficiency (PCE) of 15.6% measured from an aperture area of ~10.36 cm^2, corresponding to an active-area module PCE of 17.9% with a geometric fill factor of ~87.3%.[144]

A translucent color-neutral perovskite mini-module on 4 cm^2, with partially ablated areas resulting in a visible light transparency from 7% to 37% with a corresponding efficiency of 5% to 13%, was recently presented.[220] The opaque modules are made translucent by applying an additional patterning step P4 in a stripe design. The P4 lines remove four layers from the bottom contact up to the ETL and are perpendicularly oriented to the interconnection lines.

First tandem solar modules with notable efficiencies have been reported recently. Jaysankar *et al.* presented a semitransparent $MAPbI_3$ perovskite mini-module made from 4 monolithically interconnected cells on the 4 cm^2 area with an efficiency of 12.0% and an average transmission of 70% in the important wavelength range of 800–1200 nm through the top cell. The overall 4 T tandem efficiency was 20.2% in combination with a Si IBC cell.[253] These values could be improved to 15.3% for the semitransparent perovskite module consisting of 7 monolithically interconnected cells by both switching to the CsFAPbIBr absorber material and by advanced optical light management minimizing overall reflection and sub-bandgap transmission.[237] These improvements lead to an overall efficiency of the tandem solar module with an Si IBC cell of 23.9 cm^2 on 4 cm^2.[237]

While the above-mentioned approaches combined perovskite modules with Si single cells, the first all-thin-film 4 T modules have been demonstrated as a combination of a semitransparent $MAPbI_3$ perovskite mini-module made from 7 monolithically interconnected cells on the 3.76 cm^2 area with an efficiency of 12.0%. Combination with a CIGS module made from 4 monolithically interconnected cells leads to a 4T-tandem module with an efficiency of 17.8%,[254] exceeding the efficiencies of both submodules. These values could be improved recently to 21.3%.[255]

Flexible modules are being developed by Saule Technologies on ultrathin PET by inkjet-printing. They expect an initial efficiency of approximately 10% for DIN-A4-sized modules and an initial price of approximately 50 EUR per m^2. This would mean a LCOE (Levelized Cost of Electricity) of approximately 0.05 EUR per kWh. See Ref. 256 for a techno-economic analysis of module manufacturing.

E. Environmentally friendly approaches and stability issues

There are many approaches in the scientific community to substitute lead by non-toxic elements such as Sn,[257] Ge,[258] Bi,[259] or Cu;[260] for a review, see Refs. 261 and 262. But unfortunately, efficiencies for Pb-free perovskites continue to lag far behind the efficiencies of the Pb-containing absorber materials. The best value achieved so far for Sn-based perovskites is a record efficiency of only 9%.[263] The reasons for these poor efficiencies are amongst others: stability problems (easy oxidation of Sn^{2+} to Sn^{4+} or oxidation of Ge^{2+} to Ge^{4+}, respectively), severe carrier recombination, difficulties in controlling film morphology, and poor energy level alignment of interlayers. Interestingly, a mixture of Sn and Ge allows higher stabilities.[264] In general, partially substituting lead by tin or germanium could reduce the bandgap down to the theoretically most suitable bandgap for

single cells according to the Shockley-Queisser limit[7] or to design low-bandgap materials for use as a bottom cell tandem partner.[236,243]

By replacing the divalent Pb^{2+} by a trivalent Bi^{3+} metal cation, layered perovskites of the structure $A_3Bi_2X_9$ (A = Cs, Ag, MA; X = Cl, Br, I) are obtained. But due to the suboptimal bandgap of ca. 2 eV for $MA_3Bi_2I_9$ and poor film quality, only low efficiencies of 0.2%–3% have been achieved.[265,266]

Promising candidates for lead-free perovskites are the so-called double perovskites of the general formula $A_2M^{1+}M^{3+}X_6$. A is a monovalent cation like Cs^+, M^{1+} is for example Ag^+ or In^+, M^{3+} is Bi^{3+}, and X is a halogen (Cl^-, Br^-, or I^-). For $Cs_2AgBiBr_6$-based solar cells, a PCE of 2.4% was achieved by Greul *et al.*[267]

A major hurdle for fast commercialization of perovskite solar cells could be a limited **long-term device stability** as the original $MAPbI_3$ perovskite is water soluble and hence very prone to humidity. This issue has to be addressed in different aspects starting from fundamental material properties via optimized contact layers and suitable encapsulation strategies.

As mentioned earlier, the transition from $MAPbI_3$ perovskites to multi-cation approaches does not only improve the efficiency but also increases the moisture stability of the perovskite material. Partially replacing iodine by bromide and the use of FA can already lead to better device lifetimes.[268] A slight (5%–15%) Cs^+ incorporation into the crystal structure could stabilize the photovoltaically active trigonal phase of pure FA lead iodide ($FAPbI_3$) at room temperature.[269] The inclusion of Rb within $FAPbI_3$ leads to a higher moisture stability and already passed a 1000 h stability test at 85% r. h. in the dark without encapsulation maintaining 97% of the initial PCE.[270]

Different approaches have addressed the use of alternative interlayers or contact layers. Carbon-nanorod-functionalized polymers[271] or hydrophobic carbazoles[272] allowed higher humidity stability. Carbon-based back electrodes also generally show a higher stability.[273]

The encapsulation can be improved by using, e.g., Polytetrafluoroethylene (PTFE).[274] First publications have already demonstrated that perovskite cells can pass typical test conditions such as damp heat tests at 85 °C and 85% relative humidity for 1000 h for highly efficient cells[230] or thermal cycling for 200 cycles for EVA-encapsulated perovskite cells.[275]

F. Conclusion on perovskite cells

Industrial implementation of perovskite technology is just starting with four main companies currently active: OxfordPV, based in Oxford, UK, with module fabrication located in Germany,[276] focusing on tandem concepts in combination with Si cells; Saule Technologies based in Poland, focusing on inkjet-printed flexible cells;[277] US-based Solar-Tectic; and Microquanta Semiconductor, based in Hangzhou, China.[278]

When the major hurdles of large-area deposition, long-term stability, and possible environmental impact due to lead

contamination can be solved in a reasonable time, perovskite solar modules are expected to have huge economic potential due to their high efficiencies and low production costs. A detailed overview of economic aspects can be found, e.g., in Refs. 252 and 256. With a 15 years module lifetime, a levelized cost of electricity below 5 US cents/kW h has been estimated.[256,279]

To conclude, perovskite solar cells and modules are the technology to watch for the next decade—either as standalone technology or as efficiency-boosting add-on to silicon- or CIGS-based modules in the tandem configuration.

V. SUMMARY

Photovoltaic installations worldwide are now approaching the terawatt scale, and much more is needed to meet the demands for renewable energy now and in the future. While the great majority of installations employ conventional Si wafer-based PV modules, thin-film technologies have inherent advantages with regard to production costs, also energy cost of production, and special applications. Specifically with regard to high level mass production, and once the machinery has a higher level of standardization, the low materials usage and efficient processing workflow will enable thin-film PV to provide lower LCOE than conventional Si.

Furthermore, thin-film solar cells allow an extension of the spectrum of materials for application in future solar cells. Recent progress in the improvement of efficiencies and the development of new materials make thin-film solar cells an important option for the necessary continuous strong growth in the PV market. In particular, the possibilities to increase the area-related energy output by high-efficiency tandem cells makes PV systems more and more attractive. Variable design of modules, e.g., semitransparent structures and flexible, lightweight options, significantly extends the fields of applications. Adapting the appearance allows general integration in the infrastructure of cities and industrial buildings.

[1]See https://www.nrel.gov/pv/assets/pdfs/pv-efficiencies-07-17-2018.pdf for "NREL Research Cell Record Efficiency Chart" (2018).

[2]P. Mints, *20 Years PV from 1997–2017 Changes, Challenges, Growth Other Topics* (SPV Market Research, 2018).

[3]B. Burger, K. Kiefer, C. Kost, S. Nold, S. Philipps, R. Preu, J. Rentsch, T. Schlegl, G. Stryi-Hipp, G. Willeke, and W. Warmuth, Photovoltaics Report from August 27, 2018 (Fraunhofer Institute for Solar Energy Systems (ISE); PSE Conferences & Consulting GmbH, 2018).

[4]K. D. Dobson, I. Visoly-Fisher, G. Hodes, and D. Cahen, Sol. Energy Mater. Sol. Cells **62**, 295 (2000).

[5]J.-F. Guillemoles, U. Rau, L. Kronik, H.-W. Schock, and D. Cahen, Adv. Mater. **11**, 957 (1999).

[6]Q. Fu, X. Tang, B. Huang, T. Hu, L. Tan, L. Chen, and Y. Chen, Adv. Sci. **5**, 1700387 (2018).

[7]W. Shockley and H. J. Queisser, J. Appl. Phys. **32**, 510 (1961).

[8]B. M. Başol and B. McCandless, J. Photonics Energy **4**, 040996 (2014).

[9]P. Sinha and A. Wade, IEEE J. Photovoltaics **8**, 793 (2018).

[10]See http://www.firstsolar.com for information on production scale and status (2018).

[11]M. Gloeckler, I. Sankin, and Z. Zhao, IEEE J. Photovoltaics **3**, 1389 (2013).

[12]A. Kanevce, M. O. Reese, T. M. Barnes, S. A. Jensen, and W. K. Metzger, J. Appl. Phys. **121**, 214506 (2017).

[13]J.-H. Yang, W. K. Metzger, and S.-H. Wei, Appl. Phys. Lett. **111**, 042106 (2017).

[14]D. Guo, D. Brinkman, A. R. Shaik, C. Ringhofer, and D. Vasileska, J. Phys. D: Appl. Phys. **51**, 153002 (2018).

[15]J. D. Major, M. A. Turkestani, L. Bowen, M. Brossard, C. Li, P. Lagoudakis, S. J. Pennycook, L. J. Phillips, R. E. Treharne, and K. Durose, Nat. Commun. **7**, 13231 (2016).

[16]J. M. Burst, J. N. Duenov, D. S. Albin, E. Colegrove, M. O. Reese, J. A. Aguiar, C.-S. Jiang, M. K. Patel, M. M. Al-Jassim, D. Kuciauskas, S. Swain, T. Ablekim, K. G. Lynn, and W. K. Metzger, Nat. Energy **1**, 16015 (2016).

[17]Y. Zhao, M. Boccard, S. Liu, J. Becker, X.-H. Zhao, C. M. Campbell, E. Suarez, M. B. Lassise, Z. Holman, and Y.-H. Zhang, Nat. Energy **1**, 16067 (2016).

[18]J. J. Becker, M. Boccard, C. M. Campbell, Y. Zhao, M. Lassise, Z. C. Holman, and Y.-H. Zhang, IEEE J. Photovoltaics **7**, 900 (2017).

[19]A. H. Munshi, J. Kephart, A. Abbas, J. Raguse, J.-N. Beaudry, K. Barth, J. Sites, J. Walls, and W. Sampath, IEEE J. Photovoltaics **8**, 310 (2018).

[20]N. R. Paudel and Y. Yan, Appl. Phys. Lett. **105**, 183510 (2014).

[21]T. Baines, G. Zoppi, L. Bowen, T. P. Shalvey, S. Mariooti, K. Durose, and J. D. Major, Sol. Energy Mater. Sol. Cells **180**, 196 (2018).

[22]D. Kuciauskas, J. M. Kephart, J. Moseley, W. K. Metzger, W. S. Sampath, and P. Dippo, Appl. Phys. Lett. **112**, 263901 (2018).

[23]J. M. Burst, J. N. Duenow, A. Kanevce, H. R. Moutinho, C. S. Jiang, M. M. Al-Jassim, M. O. Reese, D. S. Albin, J. A. Aguiar, E. Colegrove, T. Ablekim, S. K. Swain, K. G. Lynn, D. Kuciauskas, T. M. Barnes, and W. K. Metzger, IEEE J. Photovoltaics **6**, 1650 (2016).

[24]X.-H. Zhao, S. Liu, C. M. Campbell, Z. Yuan, M. B. Lassise, and Y.-H. Zhang, IEEE J. Photovoltaics **7**, 913 (2017).

[25]E. S. Barnard, B. Ursprung, E. Colegrove, H. R. Moutinho, N. J. Borys, B. E. Hardin, C. H. Peters, W. K. Metzger, and P. J. Schuck, Adv. Mater. **29**, 1603801 (2017).

[26]M. A. Green, Y. Hishikawa, E. D. Dunlop, D. H. Levi, J. Hohl-Ebinger, and A. W. Y. Ho-Baillie, Prog. Photovoltaics Res. Appl. **26**, 427 (2018).

[27]See http://www.firstsolar.com/Resources/Projects/TopazSolarFarm for further information about the project.

[28]C. Gretener, J. Perrenoud, L. Kranz, E. Cheah, M. Dietrich, S. Buecheler, and A. N. Tiwari, Sol. Energy Mater. Sol. Cells **146**, 51 (2016).

[29]L. Ngan, N. Strevel, K. Passow, A. F. Panchula, and D. Jordan, in Conference on 40th IEEE PVSC, 2014.

[30]Y. Houari, J. Speirs, C. Candelise, and R. Gross, Prog. Photovoltaics Res. Appl. **22**, 129 (2014).

[31]M. Marudachalam, R. W. Birkmire, H. Hichri, J. M. Schultz, A. Swartzlander, and M. M. Al-Jassim, J. Appl. Phys. **82**, 2896 (1997).

[32]T. Kato, Jpn. J. Appl. Phys., Part 1 **56**, 04CA02 (2017).

[33]Y. Nagoya, K. Kushiya, M. Tachiyuki, and O. Yamase, Sol. Energy Mater. Sol. Cells **67**, 247 (2001).

[34]R. Lechner, in 6th International Workshop CIGS Technology, 2016.

[35]G. M. Hanket, W. N. Shafarman, and R. W. Birkmire, in *IEEE 4th World Conference Photovoltaic Energy Conference* (IEEE, 2006), pp. 560–563.

[36]I. M. Kötschau, A. Kampmann, T. Hahn, J. Hinze, E. Richter, O. Pursche, and S. Gorse, in *18th International Conference Advanced Thermal Processing Semiconductors (RTP)* (IEEE, 2010), pp. 144–144.

[37]R. A. Mickelsen and W. S. Chen, Appl. Phys. Lett. **36**, 371 (1980).

[38]A. M. Gabor, J. R. Tuttle, D. S. Albin, M. A. Contreras, R. Noufi, N. R. E. L. Golden, and Colorado, Appl. Phys. Lett. **65**, 198 (1994).

[39]A. M. Gabor, J. R. Tutle, M. H. Bode, A. Franz, A. L. Tennant, M. A. Contreras, R. Noufi, D. G. Jensen, and A. M. Hermann, Sol. Energy Mater. Sol. Cells **41-42**, 247 (1996).

[40]J. Kessler, C. Chityuttakan, J. Lu, J. Schöldström, and L. Stolt, Prog. Photovoltaics Res. Appl. **11**, 319 (2003).

[41]M. Powalla, P. Jackson, W. Witte, D. Hariskos, S. Paetel, C. Tschamber, and W. Wischmann, Sol. Energy Mater. Sol. Cells **119**, 51 (2013).

[42]K. Burrows and V. Fthenakis, Sol. Energy Mater. Sol. Cells **132**, 455 (2015).

[43]M. Edoff, T. Jarmar, N. S. Nilsson, E. Wallin, D. Hogstrom, O. Stolt, O. Lundberg, W. Shafarman, and L. Stolt, IEEE J. Photovoltaics **7**, 1789 (2017).

[44]J. Haarstrich, H. Metzner, M. Oertel, C. Ronning, T. Rissom, C. A. Kaufmann, T. Unold, H. W. Schock, J. Windeln, W. Mannstadt, and E. Rudigier, Viogt, Sol. Energy Mater. Sol. Cells **95**, 1028 (2011).

[45]*High Temperature Glass Melt Property Database Process Modeling*, edited by T. P. Seward and T. Vascott (The American Ceramic Society, Westerville, OH, 2005).

[46]T. McKittrick, "Advanced glasses their influence manufacture CIGS PV modules," in International Workshop CIGS Technology, 2011.

[47]F. Kessler and D. Rudmann, Sol. Energy **77**, 685 (2004).

[48]F. Pianezzi, S. Nishiwaki, L. Kranz, C. M. Sutter-Fella, P. Reinhard, B. Bissig, H. Hagendorfer, S. Buecheler, and A. N. Tiwari, Prog. Photovoltaics Res. Appl. **23**, 892 (2015).

[49]R. Wuerz, A. Eicke, F. Kessler, and F. Pianezzi, Sol. Energy Mater. Sol. Cells **130**, 107 (2014).

[50]K. Orgassa, H. W. Schock, and J. H. Werner, Thin Solid Films **431-432**, 387 (2003).

[51]T. Wada, N. Kohara, S. Nishiwaki, and T. Negami, Thin Solid Films **387**, 118 (2001).

[52]S. Nishiwaki, N. Kohara, T. Negami, and T. Wada, Jpn. J. Appl. Phys., Part 1 **37**, L71 (1998).

[53]X. Zhu, Z. Zhou, Y. Wang, L. Zhang, A. Li, and F. Huang, Sol. Energy Mater. Sol. Cells **101**, 57 (2012).

[54]E. Gautron, M. Tomassini, L. Arzel, and N. Barreau, Surf. Coat. Technol. **211**, 29 (2012).

[55]T. Lepetit, D. Mangin, E. Gautron, M. Tomassini, S. Harel, L. Arzel, and N. Barreau, Thin Solid Films **582**, 304 (2015).

[56]P. Blösch, S. Nishiwaki, L. Kranz, C. M. Fella, F. Pianezzi, T. Jäger, C. Adelhelm, E. Franzke, S. Buecheler, and A. N. Tiwari, Sol. Energy Mater. Sol. Cells **124**, 10 (2014).

[57]T. Dullweber, G. Hanna, U. Rau, and H. W. Schock, Sol. Energy Mater. Sol. Cells **67**, 145 (2001).

[58]N. Nicoara, T. Kunze, P. Jackson, D. Hariskos, R. F. Duarte, R. G. Wilks, W. Witte, M. Bär, and S. Sadewasser, ACS Appl. Mater. Interfaces **9**, 44173 (2017).

[59]S. Ishizuka, J. Nishinaga, M. Iioka, H. Higuchi, Y. Kamikawa, T. Koida, H. Shibata, and P. Fons, Adv. Energy Mater. **8**, 1702391 (2018).

[60]J. Kessler, K. O. Velthaus, M. Ruckh, and R. Laichinger, and H. W. Schock, in *Proceedings of the 6th International Photovoltaic Science Engineering Conference (PVSEC-6)*, New Delhi, India (1992), p. 1005.

[61]D. Hariskos, P. Jackson, W. Hempel, S. Paetel, S. Spiering, R. Menner, W. Wischmann, and M. Powalla, IEEE J. Photovoltaics **6**, 1321 (2016).

[62]M. Algasinger, T. Niesen, T. Dalibor, A. Steigert, R. Klenk, I. Lauermann, R. Schlatmann, M. C. Lux-Steiner, and J. Palm, Thin Solid Films **633**, 231 (2017).

[63]R. Klenk, A. Steigert, T. Rissom, D. Greiner, C. A. Kaufmann, T. Unold, and M. C. Lux-Steiner, Prog. Photovoltaics Res. Appl. **22**, 161 (2014).

[64]N. A. Allsop, A. Schönmann, A. Belaidi, H.-J. Muffler, B. Mertesacker, W. Bohne, E. Strub, J. Röhrich, M. C. Lux-Steiner, and C.-H. Fischer, Thin Solid Films **513**, 52 (2006).

[65]D. Hariskos, S. Spiering, and M. Powalla, Thin Solid Films **480-481**, 99 (2005).

[66]S. Siebentritt, Sol. Energy **77**, 767 (2004).

[67]K. Ellmer, Nat. Photonics **6**, 809 (2012).

[68]M. Morales-Masis, S. D. Wolf, R. Woods-Robinson, J. W. Ager, and C. Ballif, Adv. Electron. Mater. **3**, 1600529 (2017).

[69]J. Hedstrom, H. Ohlsen, M. Bodegard, A. Kylner, L. Stolt, D. Hariskos, M. Ruckh, and H.-W. Schock, in *Photovoltaic Specialist Conference PVSC 93* (1993), p. 364.

[70]K. Granath, M. Bodegard, and L. Stolt, Sol. Energy Mater. Sol. Cells **60**, 279 (2000).

[71]M. Ruckh, D. Schmid, M. Kaiser, R. Schäffler, T. Walter, and H. W. Schock, Sol. Energy Mater. Sol. Cells **41-42**, 335 (1996).

[72]A. Urbaniak, M. Igalson, F. Pianezzi, S. Bücheler, A. Chirilă, P. Reinhard, and A. N. Tiwari, Sol. Energy Mater. Sol. Cells **128**, 52 (2014).

[73]C. Persson and A. Zunger, Phys. Rev. Lett. **91**, 266401 (2003).

[74]S.-H. Wei, S. B. Zhang, and A. Zunger, J. Appl. Phys. **85**, 7214 (1999).

[75]Z.-K. Yuan, S. Chen, Y. Xie, J.-S. Park, H. Xiang, X.-G. Gong, and S.-H. Wei, Adv. Energy Mater. **6**, 1601191 (2016).

[76]O. Cojocaru-Mirédin, T. Schwarz, P.-P. Choi, M. Herbig, R. Wuerz, and D. Raabe, J. Visualized Exp. **74**, e50376 (2013).

[77]M. A. Contreras, B. Egaas, P. Dippo, J. Webb, J. Granata, K. Ramananthan, S. Asher, A. Swartzlander, and R. Noufi, in *26th PVSC IEEE Conference Proceedings* (1997).

[78]R. Wuerz, A. Eicke, F. Kessler, S. Paetel, S. Efimenko, and C. Schlegel, Sol. Energy Mater. Sol. Cells **100**, 132 (2012).

[79]D. Rudmann, D. Brémaud, H. Zogg, and A. N. Tiwari, J. Appl. Phys. **97**, 084903 (2005).

[80]A. Laemmle, R. Wuerz, and M. Powalla, Phys. Status Solidi RRL **7**, 631 (2013).

[81]A. Chirilă, P. Reinhard, F. Pianezzi, P. Bloesch, A. R. Uhl, C. Fella, L. Kranz, D. Keller, C. Gretener, H. Hagendorfer, D. Jaeger, R. Erni, S. Nishiwaki, S. Buecheler, and A. N. Tiwari, Nat. Mater. **12**, 1107 (2013).

[82]P. Jackson, D. Hariskos, R. Wuerz, W. Wischmann, and M. Powalla, Phys. Status Solidi RRL **8**, 219 (2014).

[83]D. Herrmann *et al.*, "CIGS module manufacturing with high deposition rates and efficiencies," in *2014 IEEE 40th Photovoltaic Specialist Conference (PVSC)* (Denver, CO, 2014), pp. 2775–2777.

[84]K. F. Tai, R. Kamada, T. Yagioka, T. Kato, and H. Sugimoto, Jpn. J. Appl. Phys., Part 1 **56**, 08MC03 (2017).

[85]P. Jackson, D. Hariskos, R. Wuerz, O. Kiowski, A. Bauer, T. M. Friedlmeier, and M. Powalla, Phys. Status Solidi RRL **9**, 28 (2015).

[86]P. Jackson, R. Wuerz, D. Hariskos, E. Lotter, W. Witte, and M. Powalla, Phys. Status Solidi RRL **10**, 583 (2016).

[87]See http://www.solar-frontier.com/eng/news/2017/1220_press.html for "Solar Frontier Achieves World Record Thin Film Solar Cell Efficiency 22.9%" (last accessed December 20, 2017).

[88]T. Kato, A. Handa, T. Yagioka, T. Matsuura, K. Yamamoto, S. Higashi, J.-L. Wu, K. F. Tai, H. Hiroi, T. Yoshiyama, T. Sakai, and H. Sugimoto, IEEE J. Photovoltaics **7**, 1773 (2017).

[89]T. M. Friedlmeier, P. Jackson, A. Bauer, D. Hariskos, O. Kiowski, R. Wuerz, and M. Powalla, IEEE J. Photovoltaics **5**, 1487 (2015).

[90]E. Handick, P. Reinhard, R. G. Wilks, F. Pianezzi, T. Kunze, D. Kreikemeyer-Lorenzo, L. Weinhardt, M. Blum, W. Yang, M. Gorgoi, E. Ikenaga, D. Gerlach, S. Ueda, Y. Yamashita, T. Chikyow, C. Heske, S. Buecheler, A. N. Tiwari, and M. Bär, ACS Appl. Mater. Interfaces **9**, 3581 (2017).

[91]E. Handick, P. Reinhard, J.-H. Alsmeier, L. Köhler, F. Pianezzi, S. Krause, M. Gorgoi, E. Ikenaga, N. Koch, R. G. Wilks, S. Buecheler, A. N. Tiwari, and M. Bär, ACS Appl. Mater. Interfaces **7**, 27414 (2015).

[92]Z. Z. Kish, V. B. Lazarev, E. Y. Peresh, and E. E. Semrad, "Compounds $In_2Se_3K_2Se$," Izvestiya Akademii Nauk SSSR, Neorganicheskie Materialy, **24**(10), 1602–1605 (1988); see also https://www.osti.gov/etdeweb/biblio/6194520.

[93]C. P. Muzzillo, L. M. Mansfield, K. Ramanathan, and T. J. Anderson, J. Mater. Sci. **51**, 6812 (2016).

[94]T. Lepetit, S. Harel, L. Arzel, G. Ouvrard, and N. Barreau, Prog. Photovoltaics Res. Appl. **25**, 1068 (2017).

[95]P. Pistor, D. Greiner, C. A. Kaufmann, S. Brunken, M. Gorgoi, A. Steigert, W. Calvet, I. Lauermann, R. Klenk, T. Unold, and M.-C. Lux-Steiner, Appl. Phys. Lett. **105**, 063901 (2014).

[96]M. Malitckaya, H.-P. Komsa, V. Havu, and M. J. Puska, J. Phys. Chem. C **121**, 15516 (2017).

[97]S. Ishizuka, N. Taguchi, J. Nishinaga, Y. Kamikawa, S. Tanaka, and H. Shibata, J. Phys. Chem. C **122**, 3809 (2018).

[98]A. Vilalta-Clemente, M. Raghuwanshi, S. Duguay, C. Castro, E. Cadel, P. Pareige, J. Packson, R. Wuerz, D. Hariskos, and W. Witte, Appl. Phys. Lett. **112**, 103105 (2018).

[99]S. Ishizuka, H. Shibata, J. Nishinaga, Y. Kamikawa, and P. J. Fons, Appl. Phys. Lett. **113**, 063901 (2018).

[100]F. Pianezzi, P. Reinhard, A. Chirilă, B. Bissig, S. Nishiwaki, S. Buecheler, and A. N. Tiwari, Phys. Chem. Chem. Phys. **16**, 8843 (2014).

[101]T. Feurer, B. Bissig, T. P. Weiss, R. Carron, E. Avancini, J. Löckinger, S. Buecheler, and A. N. Tiwari, Sci. Technol. Adv. Mater. **19**, 263 (2018).

[102]A. Chirilă, S. Buecheler, F. Pianezzi, P. Bloesch, C. Gretener, A. R. Uhl, C. Fella, L. Kranz, J. Perrenoud, S. Seyrling, R. Verma, S. Nishiwaki, Y. E. Romanyuk, G. Bilger, and A. N. Tiwari, Nat. Mater. **10**, 857 (2011).

[103]D. Hariskos, R. Menner, P. Jackson, S. Paetel, W. Witte, W. Wischmann, M. Powalla, L. Bürkert, T. Kolb, M. Oertel, B. Dimmler, and B. Fuchs, Prog. Photovoltaics Res. Appl. **20**, 534 (2012).

[104]T. M. Friedlmeier, P. Jackson, A. Bauer, D. Hariskos, O. Kiowski, R. Menner, R. Wuerz, and M. Powalla, Thin Solid Films **633**, 13 (2017).

[105]S. Spiering, A. Nowitzki, F. Kessler, M. Igalson, and H. A. Maksoud, Sol. Energy Mater. Sol. Cells **144**, 544 (2016).

[106]N. Barreau, J. C. Bernède, S. Marsillac, C. Amory, and W. N. Shafarman, Thin Solid Films **431-432**, 326 (2003).

[107]See https://www.avancis.de/en/press/ne for "Module Record Efficiency AVANCIS Fraunhofer ISE Certifies CIGS Solar Module Efficiency 17.9%," (last accessed February 5, 2016).

[108]S. Ishizuka, T. Koida, N. Taguchi, S. Tanaka, P. Fons, and H. Shibata, ACS Appl. Mater. Interfaces **9**, 31119 (2017).

[109]P. Bras, C. Frisk, A. Tempez, E. Niemi, and C. Platzer-Björkman, Thin Solid Films **636**, 367 (2017).

[110]G. Voorwinden, R. Kniese, and M. Powalla, Thin Solid Films **431-432**, 538 (2003).

[111]G. Voorwinden, Molekülarstrahlquellen hoher Gleichmäßigkeit: Modell und Experiment (University of Stuttgart, 2011).

[112]B. Dimmler, in International Workshop CIGS Technology, 2015.

[113]E. Niemi, J. Sterner, P. Carlsson, J. Oliv, E. Jaremalm, and S. Lindström, in 31st European Photovoltaic Solar Energy Conference Exhibition (EUPVSEC, 2015).

[114]A. Bayman, in 8th International Workshop CIGS Technology, 2017.

[115]K. Kushiya, T. Nii, I. Sugiyama, Y. Sato, Y. Inamori, and H. Takeshita, Jpn. J. Appl. Phys., Part 1 **35**, 4383 (1996).

[116]T. Dalibor and J. Palm, in 7th International Workshop CIGS Technology A new Horizon CIGS Se Efficiency Optimization: Band Gap Engineering Heterointerface, 2017.

[117]X. He, T. Paulauskas, P. Ercius, J. Varley, J. Bailey, G. Zapalac, D. Poplavskyy, N. Mackie, A. Bayman, D. Spaulding, R. Klie, V. Lordi, and A. Rockett, Sol. Energy Mater. Sol. Cells **164**, 128 (2017).

[118]K. Ellmer, J. Phys. D: Appl. Phys. **34**, 3097 (2001).

[119]S. Calnan and A. N. Tiwari, Thin Solid Films **518**, 1839 (2010).

[120]T. Koida, Y. Ueno, J. Nishinaga, H. Higuchi, H. Takahashi, M. Iioka, H. Shibata, and S. Niki, ACS Appl. Mater. Interfaces **9**, 29677 (2017).

[121]T. Koida, H. Fujiwara, and M. Kondo, Jpn. J. Appl. Phys., Part 2 **46**, L685 (2007).

[122]S. Nakano, T. Matsuoka, S. Kiyama, H. Kawata, N. Nakamura, Y. Nakashima, S. Tsuda, H. Nishiwaki, M. Hnishi, I. Nagaoka, and Y. Kuwano, Jpn. J. Appl. Phys., Part 1 **25**, 1936 (1986).

[123]R. Bartlome, B. Strahm, Y. Sinquin, A. Feltrin, and C. Ballif, Appl. Phys. B **100**, 427 (2010).

[124]A. Narazaki, T. Sato, H. Niino, H. Takada, K. Torizuka, J. Nishinaga, Y. Kamikawa-Shimizu, S. Ishizuka, H. Shibata, and S. Niki, in Laser Applications Microelectronic Optoelectronic Manufacturing (LAMOM) XXII (SPIE, 2017).

[125]T. Kato, *Recent Research Progress High-efficiency CIGS Solar Cell Solar Frontier* (at the 7th International Workshop CIGS Technology, 2016).

[126]K. Orgassa, *MANZ CIGS Technology CIGS Fab Take Off New Status Perspectives* (at the 8th International Workshop CIGS Technology, 2017).

[127]T. Dalibor, in European Photovoltaic Solar Energy Conference and Exhibition EUPVSEC, 2016.

[128]S. Nishiwaki, A. Burn, S. Buecheler, M. Muralt, S. Pilz, V. Romano, R. Witte, L. Krainer, G. J. Spühler, and A. N. Tiwari, Prog. Photovoltaics Res. Appl. **23**, 1908 (2015).

[129]J. Wennerberg, J. Kessler, and L. Stolt, Sol. Energy Mater. Sol. Cells **67**, 59 (2001).

[130]V. Probst, A. M. Lanwehr, A. Jasenek, I. Koetschau, E. Novak, P. Agoston, T. Hahn, and C. Sandfort, in SNEC Proceedings, 2015.

[131]A. Zimmermann, *Monoscribe Roll-Roll Monolithic Interconnection Customizable Thin Film Solar Modules* (at the 7th International Workshop CIGS Technology, 2016).

[132]E. Jaremalm, *Midsummer* (at the 8th International Workshop CIGS Technology, 2017).

[133]T. J. Silverman, L. Mansfield, I. Repins, and S. Kurtz, IEEE J. Photovoltaics **6**, 1333 (2016).

[134]See http://cigs-pv.net for "White Paper CIGS Thin-Film Solar Cell Technology" (2018).

[135]J. Britt, *Flexible CIGS–High Efficiency Light-Weight PV Technology* (at the 8th International Workshop CIGS Technology, 2017).

[136]Y. Sun, *The Prospect Current Status CIGS Thin Film Solar Cells China* (at the 7th International Workshop CIGS Technology, 2016).

[137]Research Analysis, *Research Report Thin Film Photovoltaics Market 2017–2030* (Roots Analysis Private Ltd., 2017).

[138]A. Bayman, in 7th International Workshop CIGS Technology, 2016.

[139]V. Bermudez, in European Photovoltaic Solar Energy Conference and Exhibition EUPVSEC, 2017.

[140]H. Sugimoto, in 8th International Workshop CIGS Technology, 2017.

[141]See http://www.solar-frontier.com/eng/news/2017/0227_press.html for "Solar Frontier's CIS Thin Film Submodule Achieves Highest Efficiency World Record 19.2%" (last accessed February 27, 2017).

[142]P. Kratzert, in European Photovoltaic Solar Energy Conference and Exhibition EUPVSEC, 2017.

[143]See https://www.pvmagazine.com/2018/02/02/hanergyssolibroAchieves1872 cigsModuleefficiencyRecord/ for "Hanergy's Solibro Achieves 18.72% CIGS Module Efficiency Record" (last accessed February 2, 2018).

[144]M. Yang, D. H. Kim, T. R. Klein, Z. Li, M. O. Reese, B. J. T. de Villers, J. J. Berry, M. F. A. M. van Hest, and K. Zhu, ACS Energy Lett. **3**, 322 (2018).

[145]A. Kojima, K. Teshima, Y. Shirai, and T. Miyasaka, J. Am. Chem. Soc. **131**, 6050 (2009).

[146]D. Zhou, T. Zhou, Y. Tian, X. Zhu, and Y. Tu, J. Nanomater. **2018**, 8148072 (2018).

[147]H. J. Snaith, J. Phys. Chem. Lett. **4**, 3623 (2013).

[148]V. M. Goldschmidt, Naturwissenschaften **14**, 477 (1926).

[149]L. T. Schelhas, J. A. Christians, J. J. Berry, M. F. Toney, C. J. Tassone, J. M. Luther, and K. H. Stone, ACS Energy Lett. **1**, 1007 (2016).

[150]N.-G. Park, Mater. Today **18**, 65 (2015).

[151]W. Hirasawa, T. Ishihara, T. Goto, K. Uchida, and N. Miura, Physica B **201**, 427 (1994).

[152]S. D. Stranks, G. E. Eperon, G. Grancini, C. Menelaou, M. J. P. Alcocer, T. Leijtens, L. M. Herz, A. Petrozza, and H. J. Snaith, Science **342**, 341 (2013).

[153]G. Xing, N. Mathews, S. Sun, S. S. Lim, Y. M. Lam, M. Grätzel, S. Mhaisalkar, and T. C. Sum, Science **342**, 344 (2013).

[154]D. W. de Quilettes, S. M. Vorpahl, S. D. Stranks, H. Nagaoka, G. E. Eperon, M. E. Ziffer, H. J. Snaith, and D. S. Ginger, Science **348**, 683 (2015).

[155]L. M. Herz, ACS Energy Lett. **2**, 1539 (2017).

[156]J. H. Noh, S. H. Im, J. H. Heo, T. N. Mandal, and S. I. Seok, Nano Lett. **13**, 1764 (2013).

[157]N. Kitazawa, Y. Watanabe, and Y. Nakamura, J. Mater. Sci. **37**, 3585 (2002).

[158]G. E. Eperon, S. D. Stranks, C. Menelaou, M. B. Johnston, L. M. Herz, and H. J. Snaith, Energy Environ. Sci. **7**, 982 (2014).

[159]R. Prasanna, A. Gold-Parker, T. Leijtens, B. Conings, A. Babayigit, H.-G. Boyen, M. F. Toney, and M. D. McGehee, J. Am. Chem. Soc. **139**, 11117 (2017).

[160]S. S. Shin, E. J. Yeom, W. S. Yang, S. Hur, M. G. Kim, J. Im, J. Seo, J. H. Noh, and S. I. Seok, Science **356**, 167 (2017).

[161]C. C. Stoumpos, C. D. Malliakas, and M. G. Kanatzidis, Inorg. Chem. **52**, 9019 (2013).

[162]E. T. Hoke, D. J. Slotcavage, E. R. Dohner, A. R. Bowring, H. I. Karunadasa, and M. D. McGehee, Chem. Sci. **6**, 613 (2015).

[163]M. C. Brennan, S. Draguta, P. V. Kamat, and M. Kuno, ACS Energy Lett. **3**, 204 (2018).

[164]J.-W. Lee, D.-H. Kim, H.-S. Kim, S.-W. Seo, S. M. Cho, and N.-G. Park, Adv. Energy Mater. **5**, 1501310 (2015).

[165]P. Yadav, M. I. Dar, N. Arora, E. A. Alharbi, F. Giordano, S. M. Zakeeruddin, and M. Grätzel, Adv. Mater. **29**, 1701077 (2017).

[166]M. Saliba, T. Matsui, K. Domanski, J.-Y. Seo, A. Ummadisingu, S. M. Zakeeruddin, J.-P. Correa-Baena, W. R. Tress, A. Abate, A. Hagfeldt, and M. Grätzel, Science **354**, 206 (2016).

[167]M. Saliba, T. Matsui, J.-Y. Seo, K. Domanski, J.-P. Correa-Baena, M. K. Nazeeruddin, S. M. Zakeeruddin, W. Tress, A. Abate, A. Hagfeldt, and M. Graetzel, Energy Environ. Sci. **9**, 1989 (2016).

[168]C. K. Moller, Nature **182**, 1436 (1958).

[169]N. J. Jeon, J. H. Noh, W. S. Yang, Y. C. Kim, S. Ryu, J. Seo, and S. I. Seok, Nature **517**, 476 (2015).

[170]D. Bi, W. Tress, M. I. Dar, P. Gao, J. Luo, C. Renevier, K. Schenk, A. Abate, F. Giordano, J.-P. C. Baena *et al.*, Sci. Adv. **2**, e1501170 (2016).

[171]D.-Y. Son, S.-G. Kim, J.-Y. Seo, S.-H. Lee, H. Shin, D. Lee, and N.-G. Park, J. Am. Chem. Soc. **140**, 1358 (2018).

[172]J. Xu, A. Buin, A. H. Ip, W. Li, O. Voznyy, R. Comin, M. Yuan, S. Jeon, Z. Ning, J. J. McDowell, P. Kanjanaboos, J.-P. Sun, X. Lan, L. N. Quan, D. H. Kim, I. G. Hill, P. Maksymovych, and E. H. Sargent, Nat. Commun. **6**, 7081 (2015).

[173]T. Li, Y. Pan, Z. Wang, Y. Xia, Y. Chen, and W. Huang, J. Mater. Chem. A **5**, 12602 (2017).

[174]J. Burschka, N. Pellet, S.-J. Moon, R. Humphry-Baker, P. Gao, M. K. Nazeeruddin, and M. Grätzel, Nature **499**, 316 (2013).

[175]V. K. LaMer and R. H. Dinegar, J. Am. Chem. Soc. **72**, 4847 (1950).

[176]B. Conings, A. Babayigit, M. T. Klug, S. Bai, N. Gauquelin, N. Sakai, J. T.-W. Wang, J. Verbeeck, H.-G. Boyen, and H. J. Snaith, Adv. Mater. **28**, 10701 (2016).

[177]N. J. Jeon, J. H. Noh, Y. C. Kim, W. S. Yang, S. Ryu, and S. I. Seok, Nat. Mater. **13**, 897 (2014).

[178]M. Xiao, F. Huang, W. Huang, Y. Dkhissi, Y. Zhu, J. Etheridge, A. Gray-Weale, U. Bach, Y.-B. Cheng, and L. Spiccia, Angew. Chem. Int. Ed. **53**, 9898 (2014).

[179]Y. Zhou, M. Yang, W. Wu, A. L. Vasiliev, K. Zhu, and N. P. Padture, J. Mater. Chem. A **3**, 8178 (2015).

[180]Z. Xiao, Q. Dong, C. Bi, Y. Shao, Y. Yuan, and J. Huang, Adv. Mater. **26**, 6503 (2014).

[181]H. Zhou, Q. Chen, G. Li, S. Luo, T. Song, H.-S. Duan, Z. Hong, J. You, Y. Liu, and Y. Yang, Science **345**, 542 (2014).

[182]A. Dubey, N. Adhikari, S. Mabrouk, F. Wu, K. Chen, S. Yang, and Q. Qiao, J. Mater. Chem. A **6**, 2406 (2018).

[183]J. Troughton, D. Bryant, K. Wojciechowski, M. J. Carnie, H. Snaith, D. A. Worsley, and T. M. Watson, J. Mater. Chem. A **3**, 9141 (2015).

[184]F. Fu, T. Feurer, T. P. Weiss, S. Pisoni, E. Avancini, C. Andres, S. Buecheler, and A. N. Tiwari, Nat. Energy **2**, 16190 (2016).

[185]W. S. Yang, B.-W. Park, E. H. Jung, N. J. Jeon, Y. C. Kim, D. U. Lee, S. S. Shin, J. Seo, E. K. Kim, J. H. Noh, and S. I. Seok, Science **356**, 1376 (2017).

[186]Q. Jiang, C. Zema, W. Pengyang, Y. Xiaolei, L. Heng, W. Ye, Y. Zhigang, W. Jinliang, Z. Xingwang, and Y. Jingbi, Adv. Mater. **29**, 1703852 (2017).

[187]D. Bi, C. Yi, J. Luo, J.-D. Décoppet, F. Zhang, S. M. Zakeeruddin, X. Li, A. Hagfeldt, and M. Grätzel, Nat. Energy **1**, 16142 (2016).

[188]K. T. Cho, S. Paek, G. Grancini, C. Roldán-Carmona, P. Gao, Y. Lee, and M. K. Nazeeruddin, Energy Environ. Sci. **10**, 621 (2017).

[189]Y. Hou, X. Du, S. Scheiner, D. P. McMeekin, Z. Wang, N. Li, M. S. Killian, H. Chen, M. Richter, I. Levchuk, N. Schrenker, E. Spiecker, T. Stubhan, N. A. Luechinger, A. Hirsch, P. Schmuki, H.-P. Steinrück, R. H. Fink, M. Halik, H. J. Snaith, and C. J. Brabec, Science **358**, 1192 (2017).

[190]N. Arora, M. I. Dar, A. Hinderhofer, N. Pellet, F. Schreiber, S. M. Zakeeruddin, and M. Grätzel, Science **358**, 768 (2017).

[191]T. Singh and T. Miyasaka, Adv. Energy Mater. **8**, 1700677 (2018).

[192]M. A. Haque, A. D. Sheikh, X. Guan, and T. Wu, Adv. Energy Mater. **7**, 1602803 (2017).

[193]U. Bach, D. Lupo, P. Comte, J. E. Moser, F. Weissörtel, J. Salbeck, H. Spreitzer, and M. Grätzel, Nature **395**, 583 (1998).

[194]P. Vivo, J. K. Salunke, and A. Priimagi, Materials **10**, 1087 (2017).

[195]L. Meng, J. You, T.-F. Guo, and Y. Yang, Acc. Chem. Res. **49**, 155 (2016).

[196]J.-Y. Jeng, Y.-F. Chiang, M.-H. Lee, S.-R. Peng, T.-F. Guo, P. Chen, and T.-C. Wen, Adv. Mater. **25**, 3727 (2013).

[197]C. Bi, Q. Wang, Y. Shao, Y. Yuan, Z. Xiao, and J. Huang, Nat. Commun. **6**, 7747 (2015).

[198]J.-Y. Jeng, K.-C. Chen, T.-Y. Chiang, P.-Y. Lin, T.-D. Tsai, Y.-C. Chang, T.-F. Guo, P. Chen, T.-C. Wen, and Y.-J. Hsu, Adv. Mater. **26**, 4107 (2014).

[199]J. You, L. Meng, T.-B. Song, T.-F. Guo, Y. M. Yang, W.-H. Chang, Z. Hong, H. Chen, H. Zhou, Q. Chen, Y. Liu, N. De Marco, and Y. Yang, Nat. Nanotechnol. **11**, 75 (2016).

[200]X. Liu, H. Yu, L. Yan, Q. Dong, Q. Wan, Y. Zhou, B. Song, and Y. Li, ACS Appl. Mater. Interfaces **7**, 6230 (2015).

[201]C.-H. Chiang, M. K. Nazeeruddin, M. Gratzel, and C.-G. Wu, Energy Environ. Sci. **10**, 808 (2017).

[202]M. Stolterfoht, C. M. Wolff, Y. Amir, A. Paulke, L. Perdigón-Toro, P. Caprioglio, and D. Neher, Energy Environ. Sci. **10**, 1530 (2017).

[203]X. Zheng, B. Chen, J. Dai, Y. Fang, Y. Bai, Y. Lin, H. Wei, X. C. Zeng, and J. Huang, Nat. Energy **2**, 17102 (2017).

[204]M. Saliba, Science **359**, 388 (2018).

[205]W. Tress, N. Marinova, T. Moehl, S. Zakeeruddin, M. K. Nazeeruddin, and M. Grätzel, Energy Environ. Sci. **8**, 995 (2015).

[206]M. De Bastiani, G. Dell'Erba, M. Gandini, V. D'Innocenzo, S. Neutzner, A. R. S. Kandada, G. Grancini, M. Binda, M. Prato, J. M. Ball, M. Caironi, and A. Petrozza, Adv. Energy Mater. **6**, 1501453 (2016).

[207]C. Eames, J. M. Frost, P. R. Barnes, B. C. Oregan, A. Walsh, and M. S. Islam, Nat. Commun. **6**, 7497 (2015).

[208]S. Meloni, T. Moehl, W. Tress, M. Franckevicius, M. Saliba, Y. H. Lee, P. Gao, M. K. Nazeeruddin, S. M. Zakeeruddin, U. Rothlisberger, and M. Graetzel, Nat. Commun. **7**, 10334 (2016).

[209]O. S. Game, G. J. Buchsbaum, Y. Zhou, N. P. Padture, and A. I. Kingon, Adv. Funct. Mater. **27**, 1606584 (2017).

[210]J. M. Frost, K. T. Butler, and A. Walsh, APL Mater. **2**, 081506 (2014).

[211]E. J. Juarez-Perez, R. S. Sanchez, L. Badia, G. Garcia-Belmonte, Y. S. Kang, I. Mora-Sero, and J. Bisquert, J. Phys. Chem. Lett. **5**, 2390 (2014).

[212]Y. Shao, Z. Xiao, C. Bi, Y. Yuan, and J. Huang, Nat. Commun. **5**, 5784 (2014).

[213]S. van Reenen, M. Kemerink, and H. J. Snaith, J. Phys. Chem. Lett. **6**, 3808 (2015).

[214]C. D. Wessendorf, J. Hanisch, D. Müller, and E. Ahlswede, Solar RRL **2**, 1800056 (2018).

[215]W. Tress, J. P. Correa Baena, M. Saliba, A. Abate, and M. Graetzel, Adv. Energy Mater. **6**, 1600396 (2016).

[216]L. Kegelmann, C. M. Wolff, C. Awino, F. Lang, E. L. Unger, L. Korte, T. Dittrich, D. Neher, B. Rech, and S. Albrecht, ACS Appl. Mater. Interfaces **9**, 17245 (2017).

[217]M. T. Hörantner, P. K. Nayak, S. Mukhopadhyay, K. Wojciechowski, C. Beck, D. McMeekin, B. Kamino, G. E. Eperon, and H. J. Snaith, ACS Appl. Mater. Interfaces **3**, 1500837 (2016).

[218]G. E. Eperon, D. Bryant, J. Troughton, S. D. Stranks, M. B. Johnston, T. Watson, D. A. Worsley, and H. J. Snaith, J. Phys. Chem. Lett. **6**, 129 (2015).

[219]S. Zhang, Y. Lu, B. Lin, Y. Zhu, K. Zhang, N.-Y. Yuan, J.-N. Ding, and B. Fang, Sol. Energy Mater. Sol. Cells **170**, 178 (2017).

[220]L. Rakocevic, R. Gehlhaar, M. Jaysankar, W. Song, T. Aernouts, H. Fledderus, and J. Poortmans, J. Mater. Chem. C **6**, 3034 (2018).

[221]L. Gao, E. Zhao, S. Yang, L. Wang, Y. Li, Y. Zhao, and T. Ma, Opt. Eng. **56**, 117107 (2017).

[222]S. Pang, D. Chen, C. Zhang, J. Chang, Z. Lin, H. Yang, X. Sun, J. Mo, H. Xi, G. Han, J. Zhang, and Y. Hao, Sol. Energy Mater. Sol. Cells **170**, 278 (2017).

[223]C. Hanmandlu, C.-Y. Chen, K. M. Boopathi, H.-W. Lin, C.-S. Lai, and C.-W. Chu, ACS Appl. Mater. Interfaces **9**, 32635 (2017).

[224]F. Fu, T. Feurer, T. Jaeger, E. Avancini, B. Bissig, S. Yoon, S. Buecheler, and A. N. Tiwari, Nat. Commun. **6**, 8932 (2015).

[225]H. Shen, T. Duong, J. Peng, D. Jacobs, N. Wu, J. Gong, Y. Wu, S. K. Karuturi, X. Fu, K. Weber, X. Xiao, T. P. White, and K. Catchpole, Energy Environ. Sci. **11**, 394 (2018).

[226]B. Chen, Y. Bai, Z. Yu, T. Li, X. Zheng, Q. Dong, L. Shen, M. Boccard, A. Gruverman, Z. Holman *et al.*, Adv. Energy Mater. **6**, 1601128 (2016).

[227]C. O. Ramirez Quiroz, Y. Shen, M. Salvador, K. Forberich, N. Schrenker, G. D. Spyropoulos, T. Heumuller, B. Wilkinson, T. Kirchartz, E. Spiecker, P. J. Verlinden, X. Zhang, M. A. Green, A. Ho-Baillie, and C. J. Brabec, J. Mater. Chem. A **6**, 3583 (2018).

[228]G. E. Eperon, T. Leijtens, K. A. Bush, R. Prasanna, T. Green, J. T.-W. Wang, D. P. McMeekin, G. Volonakis, R. L. Milot, R. May, A. Palmstrom, D. J. Slotcavage, R. A. Belisle, J. B. Patel, E. S. Parrott, R. J. Sutton, F. Wenand Moghadam Ma, B. Conings, A. Babayigit, H.-G. Boyen, S. Bent, F. Giustino, L. M. Herz, M. B. Johnston, M. D. McGehee, and H. J. Snaith, Science **354**, 861 (2016).

[229]T. Duong, Y. Wu, H. Shen, J. Peng, X. Fu, D. Jacobs, E.-C. Wang, T. C. Kho, K. C. Fong, M. Stocks, E. Franklin, A. Blakers, N. Zin, K. K. McIntosh, W. Li, Y.-B. Cheng, T. P. White, K. Weber, and K. Catchpole, Adv. Energy Mater. **7**, 1700228 (2017).

[230]K. A. Bush, A. F. Palmstrom, Z. J. Yu, M. Boccard, R. Cheacharoen, J. P. Mailoa, D. P. McMeekin, R. L. Z. Hoye, C. D. Bailie, T. Leijtens, I. M. Peters, M. C. Minichetti, N. Rolston, R. Prasanna, S. Sofia, D. Harwood, W. Ma, F. Moghadam, H. J. Snaith, T. Buonassisi, Z. C. Holman, S. F. Bent, and M. D. McGehee, Nat. Energy **2**, 17009 (2017).

[231]F. Sahli, B. A. Kamino, J. Werner, M. Bräuninger, B. Paviet-Salomon, L. Barraud, R. Monnard, J. P. Seif, A. Tomasi, Q. Jeangros, A. Hessler-Wyser, S. Wolf, M. Despeisse, S. Nicolay, B. Niesen, and C. Ballif, Adv. Energy Mater. **8**, 1701609 (2018).

[232]J. Werner, C.-H. Weng, A. Walter, L. Fesquet, J. P. Seif, S. De Wolf, B. Niesen, and C. Ballif, J. Phys. Chem. Lett. **7**, 161 (2016).

[233]J. Werner, L. Barraud, A. Walter, M. Bräuninger, F. Sahli, D. Sacchetto, N. Tétreault, B. Paviet-Salomon, S.-J. Moon, C. Allebé, M. Despeisse, S. Nicolay, S. De Wolf, B. Niesen, and C. Ballif, ACS Energy Lett. **1**, 474 (2016).

[234]F. Fu, S. Pisoni, T. P. Weiss, T. Feurer, A. Wäckerlin, P. Fuchs, S. Nishiwaki, L. Zortea, A. N. Tiwari, and S. Buecheler, Adv. Sci. **5**, 1700675 (2018).

[235]A. Guchhait, H. A. Dewi, S. W. Leow, H. Wang, G. Han, F. B. Suhaimi, S. Mhaisalkar, L. H. Wong, and N. Mathews, ACS Energy Lett. **2**, 807 (2017).

[236]D. Zhao, C. Wang, Z. Song, Y. Yu, C. Chen, X. Zhao, K. Zhu, and Y. Yan, ACS Energy Lett. **3**, 305 (2018).

[237]M. Jaysankar, T. Aernouts, R. Gehlhaar, J. Poortmans, and U. W. Paetzold, Energy Environ. Sci. **11**(6), 1489 (2018).

[238]Y. Wu, D. Yan, J. Peng, T. Duong, Y. Wan, S. P. Phang, H. Shen, N. Wu, C. Barugkin, X. Fu, S. Surve, D. Grant, D. Walter, T. P. White, K. R. Catchpole, and K. J. Weber, Energy Environ. Sci. **10**, 2472 (2017).

[239]F. Sahli, J. Werner, B. A. Kamino, M. Bräuninger, R. Monnard, B. Paviet-Salomon, L. Barraud, L. Ding, J. J. D. Leon, D. Sacchetto, G. Cattaneo, M. Despeisse, M. Boccard, S. Nicolay, Q. Jeangros, B. Niesen, and C. Ballif, Nat. Mater. **17**, 820 (2018).

[240]See www.pv-tech.org "Oxford PV Takes Record Perovskite Tandem Solar Cell to 27.3% Conversion Efficiency" (last accessed June 25, 2018).

[241]T. Todorov, T. Gershon, O. Gunawan, Y. S. Lee, C. Sturdevant, L.-Y. Chang, and S. Guha, Adv. Energy Mater. **5**, 1500799 (2015).

[242]Y. H. Jang, J. M. Lee, J. W. Seo, I. Kim, and D.-K. Lee, J. Mater. Chem. A **5**, 19439 (2017).

[243]A. Rajagopal, Z. Yang, S. B. Jo, I. L. Braly, P.-W. Liang, H. W. Hillhouse, and A. K.-Y. Jen, Adv. Mater. **29**, 1702140 (2017).

[244]C. Bi, B. Chen, H. Wei, S. DeLuca, and J. Huang, Adv. Mater. **29**, 1605900 (2017).

[245]J.-Y. Lam, J.-Y. Chen, P.-C. Tsai, Y.-T. Hsieh, C.-C. Chueh, S.-H. Tung, and W.-C. Chen, RSC Adv. **7**, 54361 (2017).

[246]X. Hu, Z. Huang, X. Zhou, P. Li, Y. Wang, Z. Huang, M. Su, W. Ren, F. Li, M. Li, Y. Chen, and Y. Song, Adv. Mater. **29**, 1703236 (2017).

[247]J. Yoon, H. Sung, G. Lee, W. Cho, N. Ahn, H. S. Jung, and M. Choi, Energy Environ. Sci. **10**, 337 (2017).

[248]Z. Liu, P. You, C. Xie, G. Tang, and F. Yan, Nano Energy **28**, 151 (2016).

[249]W. Chen, Y. Wu, Y. Yue, J. Liu, W. Zhang, X. Yang, H. Chen, E. Bi, I. Ashraful, M. Grätzel, and L. Han, Science **350**, 944 (2015).

[250]M. A. Green, K. Emery, Y. Hishikawa, W. Warta, and E. D. Dunlop, Prog. Photovoltaics Res. Appl. **23**, 805 (2015).

[251]L. K. Ono and Y. Qi, J. Phys. D: Appl. Phys. **51**, 093001 (2018).

[252]Z. Yang, S. Zhang, L. Li, and W. Chen, J. Materiomics **3**, 231 (2017).

[253]M. Jaysankar, T. Aernouts, R. Gehlhaar, U. W. Paetzold, and J. Poortmans, Adv. Energy Mater. **7**, 1602807 (2017).

[254]U. W. Paetzold, M. Jaysankar, R. Gehlhaar, E. Ahlswede, S. Paetel, W. Qiu, J. Bastos, L. Rakocevic, B. S. Richards, T. Aernouts, M. Powalla, and J. Poortmans, J. Mater. Chem. A **5**, 9897 (2017).

[255]J. P. M. Jaysankar, R. Gelhaar, M. Debucquoy, T. Aernouts, and P. Pieters, in SNEC, 2018.

[256]Z. Song, C. L. McElvany, A. B. Phillips, I. Celik, P. W. Krantz, S. C. Watthage, G. K. Liyanage, D. Apul, and M. J. Heben, Energy Environ. Sci. **10**, 1297 (2017).

[257]Z. Zhao, F. Gu, Y. Li, W. Sun, S. Ye, H. Rao, Z. Liu, Z. Bian, and C. Huang, Adv. Sci. **4**, 1700204 (2017).

[258]C. C. Stoumpos, L. Frazer, D. J. Clark, Y. S. Kim, S. H. Rhim, A. J. Freeman, J. B. Ketterson, J. I. Jang, and M. G. Kanatzidis, J. Am. Chem. Soc. **137**, 6804 (2015).

[259]B.-W. Park, B. Philippe, X. Zhang, H. Rensmo, G. Boschloo, and E. M. Johansson, Adv. Mater. **27**, 6806 (2015).

[260]X.-P. Cui, K.-J. Jiang, J.-H. Huang, Q.-Q. Zhang, M.-J. Su, L.-M. Yang, Y.-L. Song, and X.-Q. Zhou, Synth. Met. **209**, 247 (2015).

[261]A. Abate, Joule **1**, 659 (2017).

[262]A. M. Ganose, C. N. Savory, and D. O. Scanlon, Chem. Commun. **53**, 20 (2017).

[263]S. Shao, J. Liu, G. Portale, H.-H. Fang, G. R. Blake, G. H. ten Brink, L. J. A. Koster, and M. A. Loi, Adv. Energy Mater. **8**, 1702019 (2018).

[264]N. Ito, M. A. Kamarudin, D. Hirotani, Y. Zhang, Q. Shen, Y. Ogomi, S. Iikubo, T. Minemoto, K. Yoshino, and S. Hayase, J. Phys. Chem. Lett. **9**, 1682 (2018).

[265]Z. Zhang, X. Li, X. Xia, Z. Wang, Z. Huang, B. Lei, and Y. Gao, J. Phys. Chem. Lett. **8**, 4300 (2017).

[266]S. M. Jain, D. Phuyal, M. L. Davies, M. Li, B. Philippe, C. D. Castro, Z. Qiu, J. Kim, T. Watson, W. C. Tsoi, O. Karis, H. Rensmo, G. Boschloo, T. Edvinsson, and J. R. Durrant, Nano Energy **49**, 614 (2018).

[267]E. Greul, M. Petrus, A. Binek, P. Docampo, and T. Bein, J. Mater. Chem. A **5**, 19972 (2017).

[268]M. Long, T. Zhang, W. Xu, X. Zeng, F. Xie, Q. Li, Z. Chen, F. Zhou, K. S. Wong, K. Yan, and J. Xu, Adv. Energy Mater. **7**, 1601882 (2017).

[269]Z. Li, M. Yang, J.-S. Park, S.-H. Wei, J. J. Berry, and K. Zhu, Chem. Mater. **28**, 284 (2016).

[270]Y. H. Park, I. Jeong, S. Bae, H. J. Son, P. Lee, J. Lee, C.-H. Lee, and M. J. Ko, Adv. Funct. Mater. **27**, 1605988 (2017).

[271]S. N. Habisreutinger, T. Leijtens, G. E. Eperon, S. D. Stranks, R. J. Nicholas, and H. J. Snaith, Nano Lett. **14**, 5561 (2014).

[272]T. Leijtens, T. Giovenzana, S. N. Habisreutinger, J. S. Tinkham, N. K. Noel, B. A. Kamino, G. Sadoughi, A. Sellinger, and H. J. Snaith, ACS Appl. Mater. Interfaces **8**, 5981 (2016).

[273]J. Duan, T. Hu, Y. Zhao, B. He, and Q. Tang, Angew. Chem. Int. Ed. **57**, 5746 (2018).

[274]I. Hwang, I. Jeong, J. Lee, M. J. Ko, and K. Yong, ACS Appl. Mater. Interfaces **7**, 17330 (2015).

[275]R. Cheacharoen, N. Rolston, D. Harwood, K. A. Bush, R. H. Dauskardt, and M. D. McGehee, Energy Environ. Sci. **11**, 144 (2018).

[276]See www.oxfordpv.com for information on perovskite tandem module fabrication (last accessed April 2, 2018).

[277]See www.sauletech.com for information on ink-jet printed flexible perovskite cells (last accessed April 2, 2018).

[278]See Microquanta.com for information on commercializing perovskite solar cells (last accessed April 2, 2018).

[279]M. Cai, Y. Wu, H. Chen, X. Yang, Y. Qiang, and L. Han, Adv. Sci. **4**, 1600269 (2017).

[280]W. S. Yang, J. H. Noh, N. J. Jeon, Y. C. Kim, S. Ryu, J. Seo, and S. I. Seok, Science **348**, 1234 (2015).

[281]D.-Y. Son, J.-W. Lee, Y. J. Choi, I.-H. Jang, S. Lee, P. J. Yoo, H. Shin, N. Ahn, M. Choi, D. Kim, and N.-G. Park, Nat. Energy **1**, 16081 (2016).

[282]Y. C. Kim, N. J. Jeon, J. H. Noh, W. S. Yang, J. Seo, J. S. Yun, A. Ho-Baillie, S. Huang, M. A. Green, J. Seidel *et al.*, Adv. Energy Mater. **6**, 1502104 (2016).

[283]F. Zhang, Z. Wang, H. Zhu, N. Pellet, J. Luo, C. Yi, X. Liu, H. Liu, S. Wang, X. Li, Y. Xiao, S. M. Zakeeruddin, D. Bi, and M. Grätzel, Nano Energy **41**, 469 (2017).

[284]M. Abdi-Jalebi, Z. Andaji-Garmaroudi, S. Cacovich, C. Stavrakas, B. Philippe, J. M. Richter, M. Alsari, E. P. Booker, E. M. Hutter, A. J. Pearson, S. Lilliu, T. J. Savenije, H. Rensmo, G. Divitini, C. Ducati, R. H. Friend, and S. D. Stranks, Nature **555**, 497 (2018).

[285]E. H. Anaraki, A. Kermanpur, L. Steier, K. Domanski, T. Matsui, W. Tress, M. Saliba, A. Abate, M. Grätzel, A. Hagfeldt, and J.-P. Correa-Baena, Energy Environ. Sci. **9**, 3128 (2016).

[286]C. Momblona, L. Gil-Escrig, E. Bandiello, E. M. Hutter, M. Sessolo, K. Lederer, J. Blochwitz-Nimoth, and H. J. Bolink, Energy Environ. Sci. **9**, 3456 (2016).

[287]H. Tan, A. Jain, O. Voznyy, X. Lan, F. P. G. de Arquer, J. Z. Fan, R. Quintero-Bermudez, M. Yuan, F. Boand Zhao Yichengand Fan Zhang, P. Li, L. N. Quan, Y. Zhao, Z.-H. Lu, Z. Yang, S. Hoogland, and E. H. Sargent, Science **355**, 722 (2017).

[288]X. Zhu, D. Yang, R. Yang, B. Yang, Z. Yang, X. Ren, J. Zhang, J. Niu, J. Feng, and S. F. Liu, Nanoscale **9**, 12316 (2017).

[289]D. Yang, R. Yang, K. Wang, C. Wu, X. Zhu, J. Feng, X. Ren, G. Fang, S. Priya, and S. Liu, Nat. Commun. **9**, 3239 (2018).

[290]Y. Shao, Y. Yuan, and J. Huang, Nat. Energy **1**, 15001 (2016).

[291]Q. Wang, Q. Dong, T. Li, A. Gruverman, and J. Huang, Adv. Mater. **28**, 6734 (2016).

[292]Y. Lin, L. Shen, J. Dai, Y. Deng, Y. Wu, Y. Bai, X. Zheng, J. Wang, Y. Fang, H. Wei *et al.*, Adv. Mater. **29**, 1604545 (2016).

[293]S. Ye, H. Rao, Z. Zhao, L. Zhang, H. Bao, W. Sun, Y. Li, F. Gu, J. Wang, Z. Liu, Z. Bian, and C. Huang, J. Am. Chem. Soc. **139**, 7504 (2017).

[294]D. Luo, W. Yang, Z. Wang, A. Sadhanala, Q. Hu, R. Su, R. Shivanna, G. F. Trindade, J. F. Watts, Z. Xu, T. Liu, K. Chen, F. Ye, P. Wu, L. Zhao, J. Wu, Y. Tu, Y. Zhang, X. Yang, W. Zhang, R. H. Friend, Q. Gong, H. J. Snaith, and R. Zhu, Science **360**, 1442 (2018).

[295]F. Zhang, J. Song, R. Hu, Y. Xiang, J. He, Y. Hao, J. Lian, B. Zhang, P. Zeng, and J. Qu, Small **14**, 1704007 (2018).